Finite element methods for a class of continuum models for immiscible flows with moving contact lines

Arnold Reusken[1], Xianmin Xu[2] and Liang Zhang[1],*,†

[1]*Institut für Geometrie und Praktische Mathematik, RWTH Aachen University, D-52056 Aachen, Germany*
[2]*LSEC, Insitute of Computational Mathematics and Scientific/Engineering Computing, NCMIS, AMSS, Chinese Academy of Sciences, Beijing 100190, China*

SUMMARY

In this paper, we present a finite element method for two-phase incompressible flows with moving contact lines. We use a sharp interface Navier–Stokes model for the bulk phase fluid dynamics. Surface tension forces, including Marangoni forces and viscous interfacial effects, are modeled. For describing the moving contact lines, we consider a class of continuum models that contains several special cases known from the literature. For the whole model, describing bulk fluid dynamics, surface tension forces, and contact line forces, we derive a variational formulation and a corresponding energy estimate. For handling the evolving interface numerically, the level-set technique is applied. The discontinuous pressure is accurately approximated by using a stabilized extended finite element space. We apply a Nitsche technique to weakly impose the Navier slip conditions on the solid wall. A unified approach for discretization of the (different types of) surface tension forces and contact line forces is introduced. Results of numerical experiments are presented, which illustrate the performance of the solver. Copyright © 2016 John Wiley & Sons, Ltd.

1. INTRODUCTION

Two-phase flows with moving contact lines (MCL) are very common in nature and industry, for example, droplet spreading, coating flows, and two-phase flows in porous media. It is well known that the standard no-slip boundary condition will cause non-physical infinite dissipation near the moving contact line [1]. There are several ideas on how to resolve this dissipation singularity. A very popular approach is to use slip type boundary conditions close to the contact line [2]. Another possibility is to assume some thin layer of surface flow [3]. Yet another approach is to use a diffuse interface model coupled with a no-slip boundary condition [4, 5]. Besides these basic approaches, there is a wide range of other MCL models available [6–10]. For an efficient and accurate simulation of such MCL models, computational approaches that are used for two-phase flows without contact lines have to be adapted to the MCL situation [8, 11–19].

In this paper, we only consider *sharp* interface models and bulk fluids with the standard Newtonian stress tensor. We consider a *class* of sharp interface continuum models. This class is characterized by constitutive laws for the interface stress tensor σ_Γ and 'effective wall and contact line forces' $\mathbf{f}_S$, $\mathbf{f}_L$. The constitutive laws that we use are taken from the literature. For σ_Γ, we consider not only the 'clean interface model' but also models that include Marangoni effects and

---

viscous behavior (Boussinesq–Scriven) of the interface. The effective wall force $\mathbf{f}_S$ is closely related to a free-slip boundary condition on the sliding wall. The effective contact line force $\mathbf{f}_L$ results from an energy dissipation model.

Related to numerical simulation, special difficulties in this class of flow problems are the following. Because of the surface stresses, the pressure is *discontinuous* across the (moving) interface Γ. The surface stress tensor $\boldsymbol{\sigma}_\Gamma$ is *localized* on the interface and depends on the *curvature* of Γ. Often, Γ is only implicitly known (level set technique), and an accurate numerical approximation of $\boldsymbol{\sigma}_\Gamma$ is a difficult task. The effective contact line force $\mathbf{f}_L$ is *localized* on the moving contact line. An accurate numerical approximation of these surface and line forces, which is of major importance for the accuracy of the fluid dynamics simulation, is difficult to realize. Finally, the effective wall force $\mathbf{f}_S$ induces a free-slip boundary condition, and an accurate and flexible handling of this boundary condition is not straightforward.

In many papers on MCL, one uses numerical simulations for relatively simple model problems to validate the modeling approach or to illustrate certain physical phenomena, for example, [20–25]. In those papers, the focus is not on the numerical simulation methods. Other papers consider one particular numerical method, often for a restricted small class of specific models [8, 12, 15, 17, 26]. There are only very few papers that treat finite element discretization techniques specifically designed for MCL problems, for example, [27–30].

In this paper, we restrict to a (large) class of two-phase sharp interface models in which the interface and MCL modeling is based on constitutive laws for the interface stress tensor and for effective wall and contact line forces. The main contributions of this paper are a *general variational formulation* of this class of problems and the treatment of an *efficient level set based finite element discretization method*. More specifically, we will treat the following topics:

- The interface and boundary force balances that occur in the strong formulation of the model can all be treated as *natural conditions* in the variational framework. This leads to a *one-fluid variational problem* with a relatively simple structure (cf. (3.7)). This formulation determines implicitly the moving interface and the corresponding dynamic (apparent) contact angle. For this variational formulation, we derive an energy decay property.
- For tracking the implicit interface, a *level set method* is used. In this method, on the sliding wall, one does not need any special boundary conditions for the level set function.
- In the variational formulation, there are surface and contact line functionals (f_Γ and f_L in (3.7)), resulting from the natural interface and boundary conditions. We treat a *general approach for an accurate discretization of these functionals*, based on a higher order finite element approximation of the level set function.
- To deal with the pressure discontinuity, we use a *stabilized* extended finite element method (XFEM). This method has recently been introduced and analyzed in [31] for a stationary two-phase Stokes problem. We apply this method to two-phase incompressible flow problems with an MCL. As far as we know, the stabilized XFEM has not been used for this problem class, yet.
- To enhance flexibility, the no-penetration boundary condition on the sliding wall is not treated as an essential condition in the finite element space but as a natural boundary condition using *the Nitsche technique*. This Nitsche method has recently been studied in [32] for treating the Navier boundary condition in a one-phase stationary Stokes problem. We are not aware of any literature in which this technique is applied to two-phase flows with MCL.

As already noted earlier, our aim is not the comparison and/or validation of certain continuum models for contact line dynamics but to present a general variational setting to which level set, and finite element techniques are applied. The level set method that we use is a standard one. The finite element method contains several tailor-made components, as outlined earlier.

In this paper, the performance of the level set based finite element solver is studied for relatively simple 3D test problems. In future work, more difficult flows and modeling aspects will be studied.

The rest of the paper is organized as follows. In Section 2, we outline the physical background and introduce a class of models in strong formulation. A corresponding variational formulation and an energy estimate for the solution of this variational problem are presented in Section 3. In Section 4, we very briefly treat the discretization of the level set equation and the reconstruction of

the approximate interface. The three (new) numerical techniques mentioned earlier are explained in Sections 5–7. Results of numerical experiments are presented in Section 9. In Section 10, we draw conclusions and give an outlook.

2. PHYSICAL BACKGROUND AND A SHARP-INTERFACE MODEL IN STRONG FORMULATION

We introduce a sharp-interface model for immiscible two-phase flow with a moving contact line. We consider an immiscible two-phase flow in a polygonal domain $\Omega \subset \mathbb{R}^3$. The time-dependent domains of each fluid are denoted by $\Omega_1 := \Omega_1(t)$ (fluid 1) and $\Omega_2 := \Omega_2(t)$ (fluid 2). The evolving sharp interface between the two fluids is denoted by $\Gamma(t) := \partial\Omega_1 \cap \partial\Omega_2$. We assume that part of $\partial\Omega$ consists of a plane, denoted by $\partial\Omega_S$ (sliding wall) that is in contact with both fluids (cf. Figure 1). The contact line is denoted by L, and the normals on Γ and $\partial\Omega_S$ are denoted by $\mathbf{n}_\Gamma$ and $\mathbf{n}_S$, respectively. The normal to L lying in $\partial\Omega_S$ is denoted by $\mathbf{n}_L$.

We restrict to incompressible bulk fluids, and for the bulk fluid stress tensor $\boldsymbol{\sigma} = \boldsymbol{\sigma}_i(x, t)$, $i = 1, 2$, we only consider the standard Newtonian model

$$\boldsymbol{\sigma}_i := -p\mathbf{I} + \mu_i \mathbf{D}(\mathbf{u}), \quad \mathbf{D}(\mathbf{u}) := \nabla\mathbf{u} + \nabla\mathbf{u}^T, \quad i = 1, 2, \tag{2.1}$$

with p the pressure, $\mathbf{u}$ the velocity, and $\mu_i > 0$ the constant viscosity of fluid i. Mass and momentum conservation principles result in the standard Navier–Stokes equations for the fluid dynamics in the domains Ω_i, $i = 1, 2$. The interaction between the two fluids and between the fluids and the wall is described using force balances. Later, we first treat the fluid–fluid interface interaction and then the fluid–wall interaction. The latter includes the contact line modeling.

Fluid–fluid interface forces. There is extensive literature on sharp and diffusive interface models (cf. [33]). Here we restrict to sharp interface models. A standard technique [33] for the modeling of sharp interfaces is to introduce an interface stress tensor $\boldsymbol{\sigma}_\Gamma$, which acts only in planes tangential to Γ. Hence, $\boldsymbol{\sigma}_\Gamma$ has to fulfill the condition $\mathbf{P}_\Gamma \boldsymbol{\sigma}_\Gamma \mathbf{P}_\Gamma = \boldsymbol{\sigma}_\Gamma$, with the orthogonal projection $\mathbf{P}_\Gamma := \mathbf{I} - \mathbf{n}_\Gamma \mathbf{n}_\Gamma^T$. Let γ be a small connected subset of Γ with boundary $\partial\gamma$ and a normal n_γ, which is orthogonal to $\partial\gamma$ and tangential to Γ; hence, $\mathbf{P}_\Gamma n_\gamma = n_\gamma$. The stress tensor $\boldsymbol{\sigma}_\Gamma$ models the contact force in the interface Γ; that is, $\boldsymbol{\sigma}_\Gamma n_\gamma$ is the force density on $\partial\gamma$ (and thus a force per unit of length). This interface (line) contact force induces an interfacial *surface force* in Γ given by

$$\mathbf{f}_\Gamma = \text{div}_\Gamma \boldsymbol{\sigma}_\Gamma. \tag{2.2}$$

A model for $\boldsymbol{\sigma}_\Gamma$ is based on the rheology of the interface [33, 34]. A standard constitutive law is given by $\boldsymbol{\sigma}_\Gamma^0 := \tau \mathbf{P}_\Gamma$, with a (variable) surface tension coefficient $\tau > 0$, which may be a function of $x \in \Gamma$. If τ is constant, this model corresponds to a 'clean interface'. Models with a variable τ, for example, τ depending on a local surfactant concentration, lead to so-called Marangoni effects.
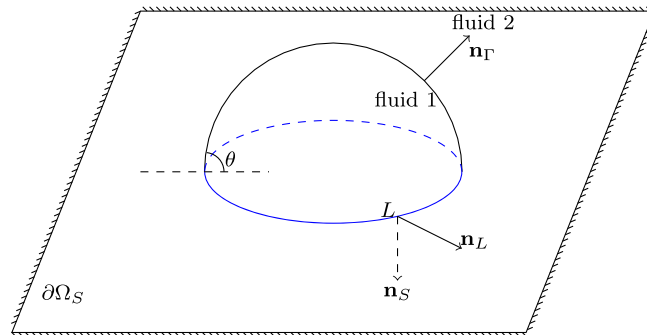

Figure 1. A liquid droplet with a contact line. [Colour figure can be viewed at wileyonlinelibrary.com]

A standard constitutive law to describe interfacial viscous forces is the following Boussinesq–Scriven model:

$$\boldsymbol{\sigma}_\Gamma^{BS} = \boldsymbol{\sigma}_\Gamma^0 + \boldsymbol{\sigma}_\Gamma^{visc}$$
$$\boldsymbol{\sigma}_\Gamma^{visc} := \lambda_\Gamma(\mathrm{div}_\Gamma \mathbf{u})\mathbf{P}_\Gamma + \mu_\Gamma \mathbf{D}_\Gamma(\mathbf{u}), \quad \mathbf{D}_\Gamma(\mathbf{u}) = \mathbf{P}_\Gamma\big(\nabla_\Gamma \mathbf{u} + (\nabla_\Gamma \mathbf{u})^T\big)\mathbf{P}_\Gamma \tag{2.3}$$

with $\lambda_\Gamma > -\mu_\Gamma$ and $\mu_\Gamma > 0$ the interface dilatational viscosity and interface shear viscosity (cf. [33]). Note the similarity to the bulk tensor model in (2.1). In the Newtonian stress tensor (2.1), the term $\mathrm{div}\,\mathbf{u}$ does not occur, because of the incompressibility assumption $\mathrm{div}\,\mathbf{u} = 0$. In general, $\mathrm{div}\,\mathbf{u} = 0$ does not imply $\mathrm{div}_\Gamma \mathbf{u} = 0$. If the interface has viscoelastic behavior, the stress tensor $\boldsymbol{\sigma}_\Gamma$ has to be adapted to this. The development of such viscoelastic surface stress tensors is an active and relatively new research area [34]. In the remainder of this paper, we only consider interface stress tensors

$$\boldsymbol{\sigma}_\Gamma \in \{\boldsymbol{\sigma}_\Gamma^0, \boldsymbol{\sigma}_\Gamma^{BS}\}.$$

We expect, however, that the (numerical) methods that are treated can also be applied (with minor modifications) to problems with other interface stress tensors.

Fluid–wall forces. There is extensive literature on the modeling of dynamic contact lines, for example, the review papers [22, 35, 36] and the references therein. One popular approach, used in, for example, [21, 26], is based on a direct relation between the contact line velocity and the dynamic apparent contact angle. Such a relation is derived in, for example, [2]. Another approach used in many papers, for example, [6, 7, 20, 22, 37–39], is based on appropriate (virtual) dissipative *effective forces* on the wall $\partial\Omega_S$ and at the contact line L. In this paper, we do not study the modeling quality of the different approaches. We restrict to the (large) class of models based on these effective forces. We outline the idea of such effective force models. The use of the conventional no-slip boundary condition $\mathbf{u} = 0$ on $\partial\Omega_S$ results in a singularity for the stress and a non-physical divergence for the energy dissipation rate (Huh and Scriven paradox [1]). Instead, on the sliding wall $\partial\Omega_S$, one typically uses the no-penetration condition $\mathbf{u} \cdot \mathbf{n}_S = 0$ combined with a free-slip boundary condition, corresponding to a tangential dissipation force $\mathbf{f}_{S,\mathrm{diss}}(\mathbf{u})$. We restrict to the simplest case that this force depends linearly on $\mathbf{u}$ and thus obtain the *effective wall force*:

$$\mathbf{f}_S = \mathbf{f}_{S,\mathrm{diss}}(\mathbf{u}) = -\beta_S \mathbf{P}_S \mathbf{u} \quad \text{on } \partial\Omega_S, \tag{2.4}$$

with $\mathbf{P}_S = \mathbf{I} - \mathbf{n}_S\mathbf{n}_S^T$, the orthogonal projection on the plane that contains $\partial\Omega_S$. We assume $\beta_S \geqslant 0$ to be a given function, depending only on $x \in \partial\Omega_S$ (e.g., constant). At the contact line, there is a wall surface tension force $(\tau_2 - \tau_1)\mathbf{n}_L$, with τ_1 and τ_2, the surface tension coefficient for wall–fluid 1 and wall–fluid 2, respectively. Using Young's equation $\tau \cos\theta_e = \tau_2 - \tau_1$, with θ_e, the static contact angle, this wall surface tension force can be reformulated as $(\tau_2 - \tau_1)\mathbf{n}_L = \tau \cos\theta_e\mathbf{n}_L$. Besides this contact line surface tension force, for a physically realistic model, one introduces a further local (i.e., at the contact line) dissipation force $\mathbf{f}_{L,\mathrm{diss}}(\mathbf{u} \cdot \mathbf{n}_L)$ [7, 20, 22]. Again, we assume the simplest case of a linear relation and thus obtain the *effective contact line force*

$$\mathbf{f}_L = \mathbf{f}_{L,\mathrm{diss}}(\mathbf{u} \cdot \mathbf{n}_L) + \tau \cos\theta_e\mathbf{n}_L = -\beta_L(\mathbf{u} \cdot \mathbf{n}_L)\mathbf{n}_L + \tau \cos\theta_e\mathbf{n}_L \quad \text{on } L, \tag{2.5}$$

where $\beta_L \geqslant 0$ is assumed to be a given function, depending only on $x \in \partial\Omega_S$ (e.g., constant). The force $\mathbf{f}_S$ is an area force density, whereas $\mathbf{f}_L$ is a line force density. Note that both forces are in the plane that contains $\partial\Omega_S$; that is, $\mathbf{P}_S\mathbf{f}_S = \mathbf{f}_S$, $\mathbf{P}_S\mathbf{f}_L = \mathbf{f}_L$. Clearly, the quality of this type of model strongly depends on the choice of the (virtual) dissipative forces $\mathbf{f}_{S,\mathrm{diss}}$ and $\mathbf{f}_{L,\mathrm{diss}}$. For a motivation and validation of this ansatz based on effective forces, using thermodynamic principles, energy arguments, and molecular dynamics (MD) simulations, we refer to the literature.

Boundary conditions. As mentioned earlier, on $\partial\Omega_S$, we assume the no-penetration condition $\mathbf{u} \cdot \mathbf{n}_S = (\mathbf{I} - \mathbf{P}_S)\mathbf{u} = 0$. On the remaining part of the boundary $\partial\Omega_D := \partial\Omega \setminus \partial\Omega_S$, we

assume no-slip boundary conditions: $\mathbf{u} = 0$ on $\partial\Omega_D$. The results of this paper apply, with minor modifications, if on $\partial\Omega_D$ we consider inhomogeneous Dirichlet boundary conditions $\mathbf{u} = \mathbf{u}_D$ instead homogeneous ones, or if on part of $\partial\Omega \setminus \partial\Omega_S$ we have a natural boundary condition $(-p\mathbf{I} + \mu\mathbf{D}(\mathbf{u}))\mathbf{n}_{\partial\Omega} = -p_{ext}\mathbf{n}_{\partial\Omega}$.

Model in strong formulation. From mass conservation and the incompressibility assumption, we obtain the equation div $\mathbf{u} = 0$ in Ω_i. With respect to momentum conservation, we assume that the only forces in the system are an external volume force (gravity) denoted by $\mathbf{g}$, viscous contact forces in the bulk phases modeled by the stress tensor $\boldsymbol{\sigma}$, interface area forces modeled by $\mathbf{f}_\Gamma = \mathrm{div}_\Gamma\boldsymbol{\sigma}_\Gamma$, and the effective wall and contact line forces $\mathbf{f}_S$, $\mathbf{f}_L$, given in (2.4) and (2.5). Momentum conservation in a material volume contained in Ω_i results in

$$\rho_i\left(\frac{\partial\mathbf{u}}{\partial t} + \mathbf{u}\cdot\nabla\mathbf{u}\right) = \mathrm{div}\,\boldsymbol{\sigma}_i + \rho_i\mathbf{g} \quad \text{in } \Omega_i,$$

where $\rho_i > 0$ denotes the constant density of the fluid in Ω_i. Momentum conservation in a material volume that is intersected by Γ (but not by $\partial\Omega_S$) yields the force balance

$$[\boldsymbol{\sigma}\mathbf{n}_\Gamma] = \mathbf{f}_\Gamma = \mathrm{div}_\Gamma\boldsymbol{\sigma}_\Gamma \quad \text{on } \Gamma,$$

with $[\cdot]$ the usual jump operator across Γ. Momentum conservation in a material volume with part of its boundary on $\partial\Omega_S$ (and no intersection with Γ) implies the force balance condition

$$\mathbf{f}_S = \mathbf{P}_S\boldsymbol{\sigma}\mathbf{n}_S = \mu\mathbf{P}_S\mathbf{D}(\mathbf{u})\mathbf{n}_S \quad \text{on } \partial\Omega_S. \tag{2.6}$$

Note that this condition, combined with the no-penetration condition $\mathbf{u}\cdot\mathbf{n}_S = 0$, is the usual Navier slip boundary condition on $\partial\Omega_S$. Similarly, using a material volume, the boundary of which is intersected by the contact line, momentum conservation implies the force balance condition

$$\mathbf{f}_L = \mathbf{P}_S\boldsymbol{\sigma}_\Gamma\boldsymbol{\tau}_L \quad \text{on } L,$$

where $\boldsymbol{\tau}_L = \frac{\mathbf{P}_\Gamma\mathbf{n}_S}{\|\mathbf{P}_\Gamma\mathbf{n}_S\|}$ is the normal to L that is tangential to Γ.

To obtain a closed model, we need further conditions. From the assumption that there is no slip at the interface and both fluids are viscous, we get $[\mathbf{u}] = 0$ on Γ. The immiscibility assumption leads to $V_\Gamma = \mathbf{u}\cdot\mathbf{n}_\Gamma$, where V_Γ denotes the normal velocity of the interface. In summary, we obtain the following *two-phase sharp interface model*

$$\begin{cases} \rho_i\left(\frac{\partial\mathbf{u}}{\partial t} + \mathbf{u}\cdot\nabla\mathbf{u}\right) = \mathrm{div}\,\boldsymbol{\sigma}_i + \rho_i\mathbf{g} \\ \mathrm{div}\,\mathbf{u} = 0, \end{cases} \quad \text{in } \Omega_i(t),\ i = 1,2, \tag{2.7}$$

$$[\boldsymbol{\sigma}\mathbf{n}_\Gamma] = \mathrm{div}_\Gamma\boldsymbol{\sigma}_\Gamma, \quad V_\Gamma = \mathbf{u}\cdot\mathbf{n}_\Gamma, \quad [\mathbf{u}] = 0 \text{ on } \Gamma(t), \tag{2.8}$$

$$\begin{cases} (\mathbf{I} - \mathbf{P}_S)\mathbf{u} = 0 \\ \mathbf{f}_S = \mathbf{P}_S\boldsymbol{\sigma}\mathbf{n}_S \end{cases} \quad \text{on } \partial\Omega_S, \tag{2.9}$$

$$\mathbf{f}_L = \mathbf{P}_S\boldsymbol{\sigma}_\Gamma\boldsymbol{\tau}_L \quad \text{on } L(t), \tag{2.10}$$

$$\mathbf{u} = 0 \quad \text{on } \partial\Omega_D. \tag{2.11}$$

For well-posedness, we in addition need suitable initial conditions for the velocity $\mathbf{u}(x, 0)$ and the initial interface $\Gamma(0)$. We are interested in the solution $\mathbf{u}(x, t)$, $p(x, t)$ (and $\Gamma(t)$) of this model, for $(x, t) \in \Omega \times [0, T]$.

Remark 2.1

We emphasize that there is still considerable freedom in the choice of the stress tensor $\boldsymbol{\sigma}_\Gamma$ and the effective wall and contact line forces $\mathbf{f}_S, \mathbf{f}_L$. In this sense, (2.7)–(2.11) form a *class* of sharp interface models. For special choices, we relate the model earlier to specific models studied in the literature. For the choice $\boldsymbol{\sigma}_\Gamma = \boldsymbol{\sigma}_\Gamma^0$, we have (cf. [40]),

$$\operatorname{div}_\Gamma \boldsymbol{\sigma}_\Gamma = \operatorname{div}_\Gamma (\tau \mathbf{P}_\Gamma) = -\tau \kappa \mathbf{n}_\Gamma + \nabla_\Gamma \tau$$

with κ, the curvature of Γ. Hence, if τ is constant, the stress tensor jump condition in (2.8) takes the familiar form $[\boldsymbol{\sigma} \mathbf{n}_\Gamma] = -\tau \kappa \mathbf{n}_\Gamma$. For this choice $\boldsymbol{\sigma}_\Gamma = \boldsymbol{\sigma}_\Gamma^0 = \tau \mathbf{P}_\Gamma$, we have $\mathbf{P}_S \boldsymbol{\sigma}_\Gamma \boldsymbol{\tau}_L = \tau \mathbf{P}_S \mathbf{P}_\Gamma \boldsymbol{\tau}_L = \tau \mathbf{P}_S \boldsymbol{\tau}_L = \tau \cos \theta \, \mathbf{n}_L$, and thus, the force balance in (2.10) takes the form

$$\beta_L U_L = \tau (\cos \theta_e - \cos \theta) \quad \text{on } L(t), \tag{2.12}$$

with $U_L := \mathbf{u} \cdot \mathbf{n}_L$ the contact line normal velocity. For $\beta_L > 0$, this relates the contact line normal velocity to the *uncompensated Young stress* or *out-of-balance interfacial tension* $\tau (\cos \theta_e - \cos \theta)$. Such a relation is studied in the literature on dynamic contact line modeling, for example, [7, 20, 22, 38]. For $\beta_L = 0$, the relation in (2.12) combined with the Navier slip boundary condition in (2.9) forms the so-called generalized Navier boundary condition (GNBC), which is treated in, for example, [6, 37, 41].

In this paper, we do not address the (important) topic of modeling the contact line dynamics in two-phase incompressible flows. In particular, we do not study which choices for the effective wall and contact line forces $\mathbf{f}_S, \mathbf{f}_L$ are (most) appropriate for certain flow problems. We note, however, that the model (2.7)–(2.11) is a macroscopic model, which implicitly determines the movement of the interface and the contact line. There does not occur any (microscopic or apparent) dynamic contact angle in this model explicitly. The resulting moving interface $\Gamma(t)$ induces a (apparent) dynamic contact angle $\theta(x, t)$, which is the angle between the sharp interface $\Gamma(t)$ and the wall $\partial \Omega_S$ (cf. Figure 1). From this observation, it follows that we can use a standard level set method for the interface capturing (cf. Section 4).

In the remainder, we focus on an elegant variational formulation of the model (2.7)–(2.11) and a general level set based finite element method that has good efficiency and robustness properties.

3. VARIATIONAL FORMULATION

In this section, we introduce a variational formulation of the model (2.7)–(2.11) introduced earlier. This variational formulation is simple in the sense that it is similar to the variational formulation of an incompressible *one*-phase Navier–Stokes equation. The reason why we obtain a relatively simple formulation is the fact that all the force balances used in (2.7)–(2.11) can be treated as *natural boundary or interface conditions* in the variational formulation.

This variational formulation forms the basis for the finite element discretization treated in the Sections 5–8. We introduce function spaces

$$\mathbf{X} := \{\mathbf{v} \in (H^1(\Omega))^3 : \mathbf{v} = \mathbf{0} \text{ on } \partial \Omega_D, \ (\mathbf{I} - \mathbf{P}_S)\mathbf{v} = 0 \text{ on } \partial \Omega_S\},$$

$$Q := \{q \in L^2(\Omega) : \int_\Omega q \, \mathrm{d}x = 0\}.$$

Note that for $\mathbf{u} \in \mathbf{X}$, the condition $[\mathbf{u}] = 0$ in (2.8) and the boundary conditions $(\mathbf{I} - \mathbf{P}_S)\mathbf{u} = 0$ (no-penetration) in (2.9) and $\mathbf{u} = 0$ (Dirichlet BC) in (2.11) are satisfied by definition of the space $\mathbf{X}$ (i.e., essential boundary conditions). It is well known that the force balance $\mathbf{f}_S = -\beta_S \mathbf{P}_S \mathbf{u} = \mathbf{P}_S \boldsymbol{\sigma} \mathbf{n}_S$ in the Navier boundary condition (2.9) can be treated as a natural boundary condition in the variational setting. We will see that the same holds for the force balances $[\boldsymbol{\sigma} \mathbf{n}_\Gamma] = \operatorname{div}_\Gamma \boldsymbol{\sigma}_\Gamma$ (on Γ) and $\mathbf{f}_L = \mathbf{P}_S \boldsymbol{\sigma}_\Gamma \boldsymbol{\tau}_L$ (on L).

It is instructive to give a derivation of the variational formulation. We multiply the Navier–Stokes equation in (2.7) by a sufficiently smooth test vector function $\mathbf{v}$ with $\mathbf{v} = 0$ on $\partial \Omega_D$ and integrate over Ω_i. We do the integration by parts

$$\int_{\Omega_i} \operatorname{div} \boldsymbol{\sigma}_i \cdot \mathbf{v} \, \mathrm{d}x = -\frac{1}{2} \int_{\Omega_i} \mu_i \mathbf{D}(\mathbf{u}) : \mathbf{D}(\mathbf{v}) \, \mathrm{d}x + \int_{\Omega_i} p \operatorname{div} \mathbf{v} \, \mathrm{d}x + \int_{\partial\Omega_i} \boldsymbol{\sigma}_i \mathbf{n}_{\Omega_i} \cdot \mathbf{v} \, \mathrm{d}s.$$

The boundary $\partial\Omega_i$ is split into three parts $\partial\Omega_i \cap \partial\Omega_D$, $\partial\Omega_i \cap \partial\Omega_S$, and $\partial\Omega_i \cap \Gamma = \Gamma$. We have either $\partial\Omega_i \cap \partial\Omega_D = \emptyset$ or $\mathbf{v} = 0$ on $\partial\Omega_i \cap \partial\Omega_D$. Hence, $\int_{\partial\Omega_i \cap \partial\Omega_D} \boldsymbol{\sigma}_i \mathbf{n}_{\Omega_i} \cdot \mathbf{v} \, \mathrm{d}s = 0$. On $\partial\Omega_S$, we write $\mathbf{v} = \mathbf{P}_S \mathbf{v} + (\mathbf{v} \cdot \mathbf{n}_S)\mathbf{n}_S$, and using the force balance in (2.9), we get

$$\sum_{i=1}^{2} \int_{\partial\Omega_i \cap \partial\Omega_S} \boldsymbol{\sigma}_i \mathbf{n}_{\Omega_i} \cdot \mathbf{v} \, \mathrm{d}s = \int_{\partial\Omega_S} \mathbf{P}_S \boldsymbol{\sigma} \mathbf{n}_S \cdot \mathbf{P}_S \mathbf{v} \, \mathrm{d}s + \int_{\partial\Omega_S} (\mathbf{n}_S \cdot \boldsymbol{\sigma} \mathbf{n}_S)(\mathbf{v} \cdot \mathbf{n}_S) \, \mathrm{d}s$$
$$= - \int_{\partial\Omega_S} \beta_S \mathbf{P}_S \mathbf{u} \cdot \mathbf{P}_S \mathbf{v} \, \mathrm{d}s + \int_{\partial\Omega_S} (\mathbf{n}_S \cdot \boldsymbol{\sigma} \mathbf{n}_S)(\mathbf{v} \cdot \mathbf{n}_S) \, \mathrm{d}s. \tag{3.1}$$

We now restrict to $\mathbf{v} \in \mathbf{X}$; hence, $\mathbf{v} \cdot \mathbf{n}_S = 0$ on $\partial\Omega_S$. Thus, the second term on the right hand-side vanishes, and we get

$$\sum_{i=1}^{2} \int_{\partial\Omega_i \cap \partial\Omega_S} \boldsymbol{\sigma}_i \mathbf{n}_{\Omega_i} \cdot \mathbf{v} \, \mathrm{d}s = - \int_{\partial\Omega_S} \beta_S \mathbf{P}_S \mathbf{u} \cdot \mathbf{P}_S \mathbf{v} \, \mathrm{d}s, \quad \mathbf{v} \in \mathbf{X}. \tag{3.2}$$

For the $\partial\Omega_i \cap \Gamma$ boundary part, we get, using the force balance in (2.8),

$$\sum_{i=1}^{2} \int_{\partial\Omega_i \cap \Gamma} \boldsymbol{\sigma}_i \mathbf{n}_{\Omega_i} \cdot \mathbf{v} \, \mathrm{d}s = \int_{\Gamma} [\boldsymbol{\sigma} \mathbf{n}_{\Gamma}] \cdot \mathbf{v} \, \mathrm{d}s = \int_{\Gamma} \operatorname{div}_{\Gamma} \boldsymbol{\sigma}_{\Gamma} \cdot \mathbf{v} \, \mathrm{d}s.$$

Combining these results, we obtain

$$\sum_{i=1}^{2} \int_{\Omega_i} \operatorname{div} \boldsymbol{\sigma}_i \cdot \mathbf{v} \, \mathrm{d}x = -\frac{1}{2} \int_{\Omega} \mu \mathbf{D}(\mathbf{u}) : \mathbf{D}(\mathbf{v}) \, \mathrm{d}x + \int_{\Omega} p \operatorname{div} \mathbf{v} \, \mathrm{d}x$$
$$- \int_{\partial\Omega_S} \beta_S \mathbf{P}_S \mathbf{u} \cdot \mathbf{P}_S \mathbf{v} \, \mathrm{d}s + \int_{\Gamma} \operatorname{div}_{\Gamma} \boldsymbol{\sigma}_{\Gamma} \cdot \mathbf{v} \, \mathrm{d}s, \quad \mathbf{v} \in \mathbf{X}. \tag{3.3}$$

Note that for the case $\boldsymbol{\sigma}_{\Gamma} = \boldsymbol{\sigma}_{\Gamma}^{BS}$, we need more smoothness than only $\mathbf{u} \in \mathbf{X}$, because $\boldsymbol{\sigma}_{\Gamma}$ contains a term $\nabla_{\Gamma}\mathbf{u}$. We need sufficient smoothness of $\mathbf{u}$ such that $(\nabla_{\Gamma}\mathbf{u})_{i,j} \in L^2(\Gamma)$.

In the derivation earlier, by using the integration by parts, the force balances in (2.9) and (2.8) are 'included' in the bilinear form on the right-hand side in (3.3). We treat the line force balance in (2.10) in the same way, namely, by applying integration by parts to the term $\int_{\Gamma} \operatorname{div}_{\Gamma} \boldsymbol{\sigma}_{\Gamma} \cdot \mathbf{v} \, \mathrm{d}s$ that occurs in (3.3). For any sufficiently smooth vector function $\mathbf{v}$, the identity

$$\int_{\Gamma} \operatorname{div}_{\Gamma} \boldsymbol{\sigma}_{\Gamma} \cdot \mathbf{v} \, \mathrm{d}s = - \int_{\Gamma} \boldsymbol{\sigma}_{\Gamma} : \nabla_{\Gamma}\mathbf{v} \, \mathrm{d}s + \int_{L} \boldsymbol{\sigma}_{\Gamma} \boldsymbol{\tau}_L \cdot \mathbf{v} \, \mathrm{d}s \tag{3.4}$$

holds. Using $\mathbf{v} = \mathbf{P}_S \mathbf{v} + (\mathbf{v} \cdot \mathbf{n}_S)\mathbf{n}_S$ and the contact line force balance in (2.10), we get

$$\int_{L} \boldsymbol{\sigma}_{\Gamma} \boldsymbol{\tau}_L \cdot \mathbf{v} \, \mathrm{d}s = \int_{L} \mathbf{P}_S \boldsymbol{\sigma}_{\Gamma} \boldsymbol{\tau}_L \cdot \mathbf{P}_S \mathbf{v} \, \mathrm{d}s + \int_{L} (\mathbf{n}_S \cdot \boldsymbol{\sigma}_{\Gamma} \boldsymbol{\tau}_L)(\mathbf{v} \cdot \mathbf{n}_S) \, \mathrm{d}s$$
$$= \int_{L} \mathbf{f}_L \cdot \mathbf{P}_S \mathbf{v} \, \mathrm{d}s + \int_{L} (\mathbf{n}_S \cdot \boldsymbol{\sigma}_{\Gamma} \boldsymbol{\tau}_L)(\mathbf{v} \cdot \mathbf{n}_S) \, \mathrm{d}s \tag{3.5}$$
$$= - \int_{L} \beta_L \mathbf{u} \cdot \mathbf{n}_L \, \mathbf{v} \cdot \mathbf{n}_L + \tau \cos\theta_e \, \mathbf{v} \cdot \mathbf{n}_L \, \mathrm{d}s + \int_{L} (\mathbf{n}_S \cdot \boldsymbol{\sigma}_{\Gamma} \boldsymbol{\tau}_L)(\mathbf{v} \cdot \mathbf{n}_S) \, \mathrm{d}s.$$

For $\mathbf{v} \in \mathbf{X}$, we have $\mathbf{v} \cdot \mathbf{n}_S = 0$, and thus, the third term in (3.5) vanishes. Hence, we get

$$\int_{\Gamma} \operatorname{div}_{\Gamma} \boldsymbol{\sigma}_{\Gamma} \cdot \mathbf{v} \, \mathrm{d}s = - \int_{\Gamma} \boldsymbol{\sigma}_{\Gamma} : \nabla_{\Gamma}\mathbf{v} \, \mathrm{d}s - \int_{L} \beta_L \mathbf{u} \cdot \mathbf{n}_L \, \mathbf{v} \cdot \mathbf{n}_L \, \mathrm{d}s + \cos\theta_e \int_{L} \tau \mathbf{v} \cdot \mathbf{n}_L \, \mathrm{d}s \tag{3.6}$$

in which the line force balance (2.10) is now 'included'. Again, as noted earlier, we need more regularity than only $\mathbf{u}, \mathbf{v} \in \mathbf{X}$ to guarantee that the quantities used in (3.6) are well defined.

Remark 3.1
Note that the appearance of the term $\cos \theta_e \int_L \tau \mathbf{v} \cdot \mathbf{n}_L \, ds$ in (3.6) is due to the line force balance (2.10), which in general is different from prescribing a static contact angle. Although if $\beta_L = 0$, this is very close to a static contact angle model.

For a compact representation of the variational problem, we introduce bilinear and trilinear forms and linear functionals:

$$m(\mathbf{u}, \mathbf{v}) := \int_\Omega \rho \mathbf{u} \cdot \mathbf{v} \, dx,$$

$$a(\mathbf{u}, \mathbf{v}) := \frac{1}{2} \int_\Omega \mu \mathbf{D}(\mathbf{u}) : \mathbf{D}(\mathbf{v}) \, dx + \int_{\partial \Omega_S} \beta_S \mathbf{P}_S \mathbf{u} \cdot \mathbf{P}_S \mathbf{v} \, ds + \int_L \beta_L \mathbf{u} \cdot \mathbf{n}_L \, \mathbf{v} \cdot \mathbf{n}_L \, ds,$$

$$b(\mathbf{v}, q) := -\int_\Omega (\operatorname{div} \mathbf{v}) q \, dx, \quad c(\mathbf{w}; \mathbf{u}, \mathbf{v}) := \int_\Omega \rho(\mathbf{w} \cdot \nabla) \mathbf{u} \cdot \mathbf{v} \, dx,$$

$$f_{ext}(\mathbf{v}) := \int_\Omega \rho \mathbf{g} \cdot \mathbf{v} \, dx, \quad f_\Gamma(\mathbf{u}, \mathbf{v}) := -\int_\Gamma \boldsymbol{\sigma}_\Gamma : \nabla_\Gamma \mathbf{v} \, ds,$$

$$f_L(\mathbf{v}) := \cos \theta_e \int_L \tau \mathbf{v} \cdot \mathbf{n}_L \, ds.$$

Remark 3.2
We comment on the surface tension force functional $f_\Gamma(\mathbf{u}, \mathbf{v})$. First we consider $\boldsymbol{\sigma}_\Gamma = \boldsymbol{\sigma}_\Gamma^0 = \tau \mathbf{P}_\Gamma$. Let id_Γ be the identity on Γ; that is, $\operatorname{id}_\Gamma(x) = x$ for $x \in \Gamma$. From $\nabla \operatorname{id}_\Gamma = \mathbf{I}$ and $\nabla_\Gamma = \mathbf{P}_\Gamma \nabla$, we obtain the representation

$$f_\Gamma(\mathbf{u}, \mathbf{v}) = -\int_\Gamma \tau \nabla_\Gamma \operatorname{id}_\Gamma : \nabla_\Gamma \mathbf{v} ds =: f_\Gamma^0(\mathbf{v}),$$

which is often used in the literature, for example, [40, 42–47]. A nice property of this surface tension representation is that curvature approximations are not (explicitly) needed. Note that in this case f_Γ depends only on $\mathbf{v}$; hence, it is a linear functional. For the Boussinesq–Scriven surface tension tensor, we get (cf. (2.3))

$$f_\Gamma(\mathbf{u}, \mathbf{v}) = -\int_\Gamma \boldsymbol{\sigma}_\Gamma^0 : \nabla_\Gamma \mathbf{v} \, ds - \int_\Gamma \boldsymbol{\sigma}_\Gamma^{visc} : \nabla_\Gamma \mathbf{v} \, ds$$

$$= f_\Gamma^0(\mathbf{v}) - \lambda_\Gamma \int_\Gamma (\operatorname{div}_\Gamma \mathbf{u}) \mathbf{P}_\Gamma : \nabla_\Gamma \mathbf{v} \, ds - \mu_\Gamma \int_\Gamma \mathbf{D}_\Gamma(\mathbf{u}) : \nabla_\Gamma \mathbf{v} \, ds.$$

This bilinear form is used in [48] for the numerical simulation of a two-phase flow problem with a viscous interface force (but without a contact line). Note that the viscous part results in a bilinear form, that is, depends not only on $\mathbf{v}$ but also on $\mathbf{u}$. In the solution process, this part is shifted to the left hand-side; that is, it is added to the bilinear form $a(\cdot, \cdot)$.

Although not explicit in the notation, the bilinear and trilinear forms and functionals depend on t, because of $\Gamma = \Gamma(t)$, $L = L(t)$, $\rho = \rho(x, t)$, $\mu = \mu(x, t)$. For any given $t \in [0, T]$, let $\mathbf{X}_t$ be a (possibly large) dense subspace of $\mathbf{X}_0$ such that the bilinear and trilinear forms and functionals defined earlier are well defined and continuous on $\mathbf{X}_t$. The derivation earlier (cf. (3.3) and (3.6)) leads to the following variational formulation. Find $\mathbf{u} = \mathbf{u}(\cdot, t) \in \mathbf{X}_t$, $p = p(\cdot, t) \in Q$ such that for (almost all) $t \in [0, T]$

$$\begin{cases} m(\partial_t \mathbf{u}, \mathbf{v}) + c(\mathbf{u}; \mathbf{u}, \mathbf{v}) + a(\mathbf{u}, \mathbf{v}) + b(\mathbf{v}, p) = f_{ext}(\mathbf{v}) + f_\Gamma(\mathbf{u}, \mathbf{v}) + f_L(\mathbf{v}) \\ b(\mathbf{u}, q) = 0 \end{cases} \tag{3.7}$$

for all $\mathbf{v} \in \mathbf{X}_t$, $q \in Q$. The derivation earlier, combined with standard variational arguments yields that a sufficiently smooth solution pair $(\mathbf{u}, p)$ of the variational problem (3.7) is a solution of the

strong formulation (2.7)–(2.11). In this sense, the variational problem (3.7) is consistent with the model (2.7)–(2.11). An interesting property of this formulation is that both *curvature approximations and contact angle approximations* are not needed. In the remainder of this paper, we consider the variational problem (3.7). For the special case $\sigma_\Gamma = \sigma_\Gamma^0$ with a constant τ and with $\beta_L = 0$ in (2.5), a numerical discretization method of this variational problem based on an ALE approach is presented in [27, 28]. In Sections 4–8, we present an Eulerian finite element method for the discretization of (3.7). In the next section, we first derive an energy decay property.

3.1. Energy estimate

An energy decay property of the weak formulation (3.7) is shown in this section. We assume that the surface tension coefficients τ, τ_1, τ_2 are constant. We introduce some notation. The wall boundary part in contact with fluid i is denoted by $\Gamma_S^{(i)} = \partial\Omega_i \cap \partial\Omega_S$. The area of the interfaces $\Gamma(t)$ and $\Gamma_S^{(i)}(t)$ is denoted by $|\Gamma(t)|$ and $|\Gamma_S^{(i)}(t)|$. The norm $\|\cdot\|$ denotes the Euclidean vector norm. We define the energy

$$E_{\mathbf{u}}(t) = \frac{1}{2}\int_\Omega \rho\|\mathbf{u}\|^2\,dx + \tau|\Gamma(t)| + \tau_1|\Gamma_S^{(1)}(t)| + \tau_2|\Gamma_S^{(2)}(t)|,$$

which is the sum of kinetic and surface energies.

Lemma 3.1
We assume $\mathbf{g} = 0$; that is, $f_{ext}(\mathbf{v}) = 0$. We consider $\sigma_\Gamma = \sigma_\Gamma^{BS}$. Let $(\mathbf{u}, p)$ be a solution of (3.7) for $t \in [0, T]$. The following holds:

$$\frac{d}{dt}E_{\mathbf{u}}(t) = -\left[\frac{1}{2}\int_\Omega \mu\mathrm{tr}(\mathbf{D}(\mathbf{u})^2)\,dx + \lambda_\Gamma\int_\Gamma \mathrm{tr}(\nabla_\Gamma\mathbf{u})^2\,ds + \frac{1}{2}\mu_\Gamma\int_\Gamma \mathrm{tr}(\mathbf{D}_\Gamma(\mathbf{u})^2)\,ds \right.$$
$$\left. + \int_{\partial\Omega_S} \beta_S\|\mathbf{P}_S\mathbf{u}\|^2\,ds + \int_L \beta_L(\mathbf{u}\cdot\mathbf{n}_L)^2\,ds\right]. \tag{3.8}$$

For $\sigma_\Gamma = \sigma_\Gamma^0$, the same relation holds, with $\lambda_\Gamma = \mu_\Gamma = 0$.

Proof
We choose $\mathbf{u}$ as the test function in the first equation (3.7). From the second equation, we get $b(\mathbf{u}, p) = 0$. We have

$$\frac{1}{2}\frac{d}{dt}\int_\Omega \rho\|\mathbf{u}\|^2\,dx = \frac{1}{2}\sum_{i=1}^2 \frac{d}{dt}\int_{\Omega_i(t)} \rho\|\mathbf{u}\|^2\,dx$$
$$= \frac{1}{2}\sum_{i=1}^2 \int_{\Omega_i(t)} \rho_i\frac{\partial}{\partial t}(\mathbf{u}\cdot\mathbf{u}) + \rho_i\mathbf{u}\cdot\nabla(\mathbf{u}\cdot\mathbf{u})\,dx \tag{3.9}$$
$$= \sum_{i=1}^2 \int_{\Omega_i(t)} \rho_i\frac{\partial\mathbf{u}}{\partial t}\cdot\mathbf{u} + \rho_i(\mathbf{u}\cdot\nabla\mathbf{u})\cdot\mathbf{u}\,dx = m(\partial_t\mathbf{u}, \mathbf{u}) + c(\mathbf{u}; \mathbf{u}, \mathbf{u})$$
$$= -a(\mathbf{u}, \mathbf{u}) + f_\Gamma(\mathbf{u}, \mathbf{u}) + f_L(\mathbf{u}).$$

We consider the three terms in (3.9). For the first one, we get

$$a(\mathbf{u}, \mathbf{u}) = \frac{1}{2}\int_\Omega \mu\,\mathrm{tr}(\mathbf{D}(\mathbf{u})^2)\,dx + \int_{\partial\Omega_S} \beta_S\|\mathbf{P}_S\mathbf{u}\|^2\,ds + \int_L \beta_L(\mathbf{u}\cdot\mathbf{n}_L)^2\,ds. \tag{3.10}$$

We consider the second term $f_\Gamma(\mathbf{u}, \mathbf{u})$ for $\sigma_\Gamma = \sigma_\Gamma^{BS}$. The case $\sigma_\Gamma = \sigma_\Gamma^0$ is a special case of this, with $\lambda_\Gamma = \mu_\Gamma = 0$. We use $\mathrm{div}_\Gamma\mathbf{u} = \mathrm{tr}(\nabla_\Gamma\mathbf{u}) = \mathrm{tr}(\mathbf{P}_\Gamma\nabla_\Gamma\mathbf{u}) = \mathbf{P}_\Gamma : \nabla_\Gamma\mathbf{u}$ and $\mathrm{tr}((A + A^T)A) =$

$\frac{1}{2}\mathrm{tr}\big((A + A^T)^2\big)$ for any matrix A. We obtain

$$
\begin{aligned}
f_\Gamma(\mathbf{u}, \mathbf{u}) &= -\int_\Gamma \boldsymbol{\sigma}_\Gamma^{BS} : \nabla_\Gamma \mathbf{u} \, ds \\
&= -\tau \int_\Gamma \mathbf{P}_\Gamma : \nabla_\Gamma \mathbf{u} \, ds - \lambda_\Gamma \int_\Gamma (\mathrm{div}_\Gamma \mathbf{u}) \mathbf{P}_\Gamma : \nabla_\Gamma \mathbf{u} \, ds - \mu_\Gamma \int_\Gamma \mathbf{D}_\Gamma(\mathbf{u}) : \nabla_\Gamma \mathbf{u} \, ds \\
&= -\tau \int_\Gamma \mathrm{div}_\Gamma \mathbf{u} \, ds - \lambda_\Gamma \int_\Gamma \mathrm{tr}(\nabla_\Gamma \mathbf{u})^2 \, ds - \frac{1}{2}\mu_\Gamma \int_\Gamma \mathrm{tr}\big(\mathbf{D}_\Gamma(\mathbf{u})^2\big) \, ds \\
&= -\tau \frac{d}{dt}|\Gamma(t)| - \lambda_\Gamma \int_\Gamma \mathrm{tr}(\nabla_\Gamma \mathbf{u})^2 \, ds - \frac{1}{2}\mu_\Gamma \int_\Gamma \mathrm{tr}\big(\mathbf{D}_\Gamma(\mathbf{u})^2\big) \, ds
\end{aligned}
\tag{3.11}
$$

where in the last equality we used $\int_{\Gamma(t)} \mathrm{div}_\Gamma \mathbf{u} \, ds = \frac{d}{dt}\int_{\Gamma(t)} 1 \, ds$. For treating the third term $f_L(\mathbf{u})$, we use Stokes theorem in the plane that contains the wall $\partial\Omega_S$. The divergence operator in this plane is denoted by div_S. Using $\Gamma_S^{(1)} \subset \partial\Omega_S$ and $L = \partial\Gamma_S^{(1)}$, we get

$$
\begin{aligned}
f_L(\mathbf{u}) &= \tau \cos\theta_e \int_L \mathbf{u}\cdot\mathbf{n}_L \, ds = \tau \cos\theta_e \int_{\Gamma_S^{(1)}} \mathrm{div}_S \mathbf{u} \, ds \\
&= \tau \cos\theta_e \frac{d}{dt}\int_{\Gamma_S^{(1)}(t)} 1 \, ds = \tau \cos\theta_e \frac{d}{dt}|\Gamma_S^{(1)}(t)| \\
&= -\frac{d}{dt}\big(\tau_1 |\Gamma_S^{(1)}(t)| + \tau_2 |\Gamma_S^{(2)}(t)|\big).
\end{aligned}
\tag{3.12}
$$

In the last inequality, we used Young's relation $\tau \cos\theta_e = \tau_2 - \tau_1$ and $|\Gamma_S^{(1)}(t)| + |\Gamma_S^{(2)}(t)| = |\partial\Omega_S|$ is independent of t. Combination of (3.9),(3.10),(3.11), and (3.12) completes the proof. $\square$

A similar result, for the case $\boldsymbol{\sigma}_\Gamma = \boldsymbol{\sigma}_\Gamma^0$, is derived in [20, 41]. The terms on the right hand-side in (3.8) have obvious interpretations: They correspond to bulk viscosity, interface viscosity, and wall and contact line dissipation energies. From $\mu > 0$, $\lambda_\Gamma \geqslant 0$, $\mu_\Gamma \geqslant 0$, $\beta_S \geqslant 0$, $\beta_L \geqslant 0$, it follows that there is energy decay.

Remark 3.3
The condition $\lambda_\Gamma \geqslant 0$ may not be fulfilled in certain cases. In the literature (cf. [33] Sect. 4.9.5.), also the weaker condition $\lambda_\Gamma \geqslant -\mu_\Gamma$ is used. One can show that if $\lambda_\Gamma \geqslant 0$ is replaced by $\lambda_\Gamma \geqslant -\mu_\Gamma$, one still has the energy decay property.

4. LEVEL-SET METHOD

A key difficulty in the numerical simulation of two-phase flows is the numerical approximation of the (implicitly given) interface. Different techniques are available (cf. [40] for an overview). In the numerical method used in this paper, we use the popular level set technique, which implicitly captures the position of $\Gamma(t)$. We will briefly introduce the method and explain how one can approximate the interface Γ. We introduce a time-dependent level-set function $\phi(x, t)$ such that $\Gamma(t) = \{(x, t) \mid \phi(x, t) = 0\}$. This level set function is given for $t = 0$ (e.g., an approximate distance function to $\Gamma(0)$), and its evolution is determined by the linear transport equation

$$
\frac{\partial\phi}{\partial t} + \mathbf{u}\cdot\nabla\phi = 0. \tag{4.1}
$$

On the sliding wall, for the fluid dynamics, we have the no-penetration boundary condition $\mathbf{u}\cdot\mathbf{n}_S = 0$. Furthermore, the variational model (3.7) implicitly determines the movement of the contact line. From this, it follows that for the level set equation we do not need any boundary condition for ϕ on $\partial\Omega_S$. Because of $\mathbf{u} = 0$ on $\partial\Omega_D$, the same holds for the Dirichlet boundaries. It follows that for the level set equation we do not need any modifications for the moving contact line problem, compared with a two-phase problem without contact line.

For the space discretization of this equation, we use a standard finite element approach, which we briefly outline. Let $\{\mathcal{T}_h\}_{h>0}$ be a shape regular family of tetrahedral triangulations of the domain Ω. For given boundary data ϕ_D on the inflow boundary $\partial\Omega_{in}$, we introduce the finite element space of piecewise quadratics:

$$V_h(\phi_D) = \{\, \phi_h \in C(\Omega) \mid \phi_h|_T \in \mathcal{P}_2 \text{ for all } T \in \mathcal{T}_h, \ \phi_h = \phi_D \text{ on } \partial\Omega_{in} \,\}.$$

The level set equation is semi-discretized using the streamline diffusion finite element method (SDFEM): determine $\phi_h(\cdot, t) \in V_h(\phi_D)$ such that

$$\sum_{T \in \mathcal{T}_h} \left(\frac{\partial \phi_h}{\partial t} + \mathbf{u} \cdot \nabla \phi_h, v_h + \delta_T \mathbf{u} \cdot \nabla v_h \right)_{L^2(T)} = 0 \quad \text{for all } v_h \in V_h(0), \tag{4.2}$$

where δ_T is the SDFEM stabilization parameter (cf. [49]). This parameter typically has the form $\delta_T = c \frac{h_T}{\max\{\epsilon_0, \|\mathbf{u}\|_{\infty,T}\}}$ with $\epsilon_0 > 0$ and $c = \mathcal{O}(1)$. The fact that we use quadratic (instead of linear) finite elements is essential for an accurate approximation of surface tension forces [44]. The heuristic explanation for this is that in the surface tension force the curvature of $\Gamma(t)$ plays a key role and approximation of the curvature using piecewise linears for $\phi_h(\cdot, t)$ turns out to be too inaccurate. In the discretization of the surface and line forces f_Γ and f_L in (3.7), which is explained in Section 7 later, we need an explicitly accessible approximation of $\Gamma(t)$ and an approximation of the normal n_Γ. A crucial point in our approach is that the former is based on a piecewise *linear* interpolation of the piecewise quadratic function $\phi_h(\cdot, t)$, whereas for the latter, we use the piecewise *quadratic* function. We give a more precise explanation of this approach. Computing (a parametrization of) the zero level of the piecewise quadratic function $\phi_h(\cdot, t)$ is computationally extremely expensive. Instead, we determine the piecewise linear interpolation of $\phi_h(\cdot, t)$ on the regularly refined triangulation $\mathcal{T}_{\frac{1}{2}h}$, denoted by $I\phi_h(\cdot, t)$. The approximate interface is given by

$$\Gamma_h(t) := \{\, x \in \Omega \mid I\phi_h(x, t) = 0 \,\}. \tag{4.3}$$

This approximate interface is piecewise planar (consisting of triangles an quadrilaterals) and easy to determine. Under reasonable assumptions, the estimate $\text{dist}(\Gamma, \Gamma_h) \leqslant ch^2$ holds (cf. [40]). The normals and corresponding projections needed in the numerical approximation of the force terms (cf. Section 7) are determined as follows (we delete the dependence on t in the notation):

$$\tilde{\mathbf{n}}_h := \frac{\nabla \phi_h}{\|\nabla \phi_h\|}, \quad \tilde{\mathbf{P}}_h = \mathbf{I} - \tilde{\mathbf{n}}_h \tilde{\mathbf{n}}_h^T. \tag{4.4}$$

This choice leads to significantly better results than using the normals to the piecewise planar approximation Γ_h.

Related to the numerical treatment of the level set function, there are further important issues such as reinitialization (also called reparametrization) and volume correction. We do not treat these topics in this paper. For reinitialization, we use a fast marching method as presented in [50]. For volume correction, we apply a simple shift technique. For more information about these methods, we refer to [40].

5. PRESSURE DISCRETIZATION: STABILIZED P_1-XFEM METHOD

In the two-phase problem, the normal bulk stress tensor $\sigma \mathbf{n}_\Gamma$ is discontinuous across the interface Γ (cf. (2.8)). This results in a pressure jump and a discontinuity in the velocity derivative across the interface. An accurate approximation of these discontinuities is a difficult task because, because of the use of the level set technique, the triangulation is not fitted to the (moving) interface. In particular, the discontinuity in the pressure results in very large discretization errors (of order $\sqrt{h}$ in the L^2-norm) if standard finite element spaces are used. In recent years, the XFEM technique has been successfully applied to deal with this problem. For an accurate pressure discretization, we will

use a P_1-XFEM known from the literature [31]. So far, this method has been applied to two-phase flows *without* contact lines only. We apply this method *without any modifications* to the problem with a moving contact line. We briefly explain this stabilized XFEM method.

Let $\{\mathcal{T}_h\}_{h>0}$ be the same family of shape-regular tetrahedral triangulations as for the discretization of the level set equation. The space of piecewise linears is denoted by

$$Q_h := \{q \in C(\Omega) : q|_T \in \mathcal{P}_1 \text{ for all } T \in \mathcal{T}_h\}.$$

We introduce the subdomains

$$\Omega_{i,h} := \{T \in \mathcal{T}_h : \mathrm{meas}_3(T \cap \Omega_i) > 0\}, \qquad i = 1, 2,$$

and the corresponding finite element spaces

$$Q_{i,h} := Q_{h|\Omega_{i,h}} = \{q \in C(\Omega_{i,h}) \mid q|_T \in \mathcal{P}_1 \text{ for all } T \in \Omega_{i,h}\}, \qquad i = 1, 2.$$

We define $\mathcal{T}_h^\Gamma := \{T \in \mathcal{T}_h \mid \mathrm{meas}_2(T \cap \Gamma_h) > 0\}$, which is the set of elements intersected by Γ_h. The following sets of faces are needed in the stabilization procedure (cf. Figure 2):

$$\mathcal{F}_i = \{F \subset \partial T \mid T \in \mathcal{T}_h^\Gamma, F \not\subset \partial\Omega_{i,h}\}, \ i = 1, 2,$$

and $\mathcal{F}_h := \mathcal{F}_1 \cup \mathcal{F}_2$. For each $F \in \mathcal{F}_h$, the unit normal with a fixed orientation is denoted by n_F.

A given pair $p_h = (p_{1,h}, p_{2,h}) \in Q_{1,h} \times Q_{2,h}$ may have two values for $x \in \mathcal{T}_h^\Gamma$. We define a uni-valued function $p_h^\Gamma(x) \in C(\Omega_1 \cup \Omega_2)$ by

$$p_h^\Gamma(x) = p_{i,h}(x), \qquad \text{for } x \in \Omega_i.$$

The mapping $p_h \longmapsto p_h^\Gamma$ is bijective. The P_1-XFEM space is defined by

$$Q_h^\Gamma := (Q_{1,h} \times Q_{2,h})/\mathbb{R} = \left\{ p_h \in Q_{1,h} \times Q_{2,h} \mid \int_\Omega p_h^\Gamma \, dx = 0 \right\}. \tag{5.1}$$

Note that $\{p_h^\Gamma : p_h \in Q_h^\Gamma\}$ is a subspace of the pressure space Q. The space Q_h^Γ can also be characterized as a space obtained by adding certain discontinuous basis functions, with support in $\mathcal{T}_h^\Gamma$, to the original space Q_h. This explains the name 'extended FEM'. Because of the very small areas of certain cut elements $T \cap \Omega_i$, a discretization in the space Q_h^Γ may lead to instabilities in the discrete solution and/or very poor conditioning of the stiffness matrix (cf. [31, 51]). Recently, the following ghost-penalty stabilization for P_1-XFEM has been introduced [31]:
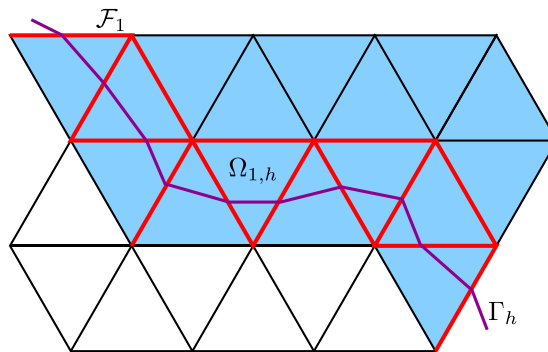

Figure 2. The subdomain $\Omega_{1,h}$ (in blue), the set of faces $\mathcal{F}_1$ (in red), and the reconstructed interface Γ_h (in purple).

$$j(p_h, q_h) = \sum_{i=1}^{2} j_i(p_{i,h}, q_{i,h}), \qquad p_h, q_h \in Q_{1,h} \times Q_{2,h},$$

$$j_i(p_{i,h}, q_{i,h}) = \mu_i^{-1} \sum_{F \in \mathcal{F}_i} h_F^3 ([\nabla p_{i,h} \cdot n_F][\nabla q_{i,h} \cdot n_F])_{0,F}, \qquad (5.2)$$

where h_F is the diameter of the face F and $[\nabla p_{i,h} \cdot n_F]$ denotes the jump of the normal components of the piecewise constant function $\nabla p_{i,h}$ across the face F. Later in Section 8, we will use the space Q_h^Γ for a conforming pressure discretization and modify the bilinear form by adding the stabilization term $\epsilon_p j(\cdot, \cdot)$ with the parameter $\epsilon_p > 0$. Note that this is a consistent stabilization, in the sense that for a piecewise continuous pressure solution p (i.e., $p_{|\Omega_i}$ is continuous) and for all $q_h \in Q_h^\Gamma$, we have $j(p, q_h) = 0$.

Another XFEM stabilization approach is presented in [51]. In that method, one deletes from the XFEM space all basis functions with a relatively very small support. In our experience, the ghost penalty method performs better. Hence, in the numerical experiments, we use the stabilization method based on (5.2).

6. VELOCITY DISCRETIZATION: NITSCHE P_2-FEM

As noted earlier, the discontinuity of $\boldsymbol{\sigma} \mathbf{n}_\Gamma$ across the interface causes a discontinuity not only in the pressure but also in the derivative of the velocity, if $\mu_1 \neq \mu_2$. Hence, if $\mu_1 \neq \mu_2$, a standard P_2 finite element space for velocity discretization does not have optimal approximation properties. Numerical experiments [40, 52] have shown that in cases with small viscosity jumps often the velocity error in the P_2-FEM space does not dominate the total discretization error. This explains why in practice the pair P_1-XFEM (with stabilization) for pressure and P_2-FEM for velocity is often used. In this paper, we also use this pair; that is, velocity is approximated in the finite element space

$$X_h := \{ \mathbf{v} \in C(\Omega) \mid \mathbf{v}|_T \in (\mathcal{P}_2)^3 \text{ for all } T \in \mathcal{T}_h, \ \mathbf{v}_{|\partial \Omega_D} = 0 \}. \qquad (6.1)$$

Note that this is not a conforming space, because the Navier boundary condition $\mathbf{n}_S \cdot \mathbf{v} = 0$ on $\partial \Omega_S$ is not an essential boundary condition in the finite element space. Often the direct imposition of this condition is not easy to implement, especially when the normal $\mathbf{n}_S$ does not have the direction of a coordinate axis (e.g., an inclined wall or a curved boundary $\partial \Omega_S$). In this paper, we show how one can use the Nitsche technique to weakly impose $\mathbf{u} \cdot \mathbf{n}_S = 0$ on the boundary $\partial \Omega_S$ [53, 54].

For this Nitsche method, we have to modify the bilinear form(s) used in the variational formulation. We recall the arguments used in Section 3. Note that the test functions $\mathbf{v} \in \mathbf{X}_h$ do not satisfy $\mathbf{v} \cdot \mathbf{n}_S = 0$. Following the arguments in Section 3, we observe that (3.1) is still correct, but now, the term $\int_{\partial \Omega_S} (\mathbf{n}_S \cdot \boldsymbol{\sigma} \mathbf{n}_S)(\mathbf{v} \cdot \mathbf{n}_S) \, ds$ does not vanish. This term can be written as

$$\int_{\partial \Omega_S} (\mathbf{n}_S \cdot \boldsymbol{\sigma} \mathbf{n}_S)(\mathbf{v} \cdot \mathbf{n}_S) \, ds = -\int_{\partial \Omega_S} p \, \mathbf{v} \cdot \mathbf{n}_S \, ds + \int_{\partial \Omega_S} \mu (\mathbf{n}_S \cdot \mathbf{D}(\mathbf{u})\mathbf{n}_S)(\mathbf{v} \cdot \mathbf{n}_S) \, ds.$$

The first term on the right hand-side will be added to the bilinear form $b(\cdot, \cdot)$, and the second term will be added to $a(\cdot, \cdot)$. Similarly, following the arguments in the second step of integration by parts (starting from (3.4)), we observe that (3.5) is still correct, but now, the term $\int_L (\mathbf{n}_S \cdot \boldsymbol{\sigma}_\Gamma \boldsymbol{\tau}_L)(\mathbf{v} \cdot \mathbf{n}_S) \, ds$ does not vanish. This term will be added to the contact line functional f_L.

Hence, in the Nitsche method, we introduce three modified bilinear forms:

$$\tilde{b}(\mathbf{v}, q) = b(\mathbf{v}, q) + \int_{\partial \Omega_S} (\mathbf{v} \cdot \mathbf{n}_S) q \, ds, \qquad (6.2)$$

$$\tilde{a}(\mathbf{u}, \mathbf{v}) := a(\mathbf{u}, \mathbf{v}) - \int_{\partial\Omega_S} \mu(\mathbf{n}_S \cdot \mathbf{D}(\mathbf{u})\mathbf{n}_S)(\mathbf{v} \cdot \mathbf{n}_S)\,\mathrm{d}s$$
$$- \int_{\partial\Omega_S} \mu(\mathbf{n}_S \cdot \mathbf{D}(\mathbf{v})\mathbf{n}_S)(\mathbf{u} \cdot \mathbf{n}_S)\,\mathrm{d}s + \frac{\alpha}{h}\int_{\partial\Omega_S}(\mathbf{u} \cdot \mathbf{n}_S)(\mathbf{v} \cdot \mathbf{n}_S)\,\mathrm{d}s, \tag{6.3}$$

$$\tilde{f}_L(\mathbf{u}, \mathbf{v}) = f_L(\mathbf{v}) + \int_L (\mathbf{n}_S \cdot \boldsymbol{\sigma}_\Gamma \boldsymbol{\tau}_L)(\mathbf{v} \cdot \mathbf{n}_S)\,\mathrm{d}s. \tag{6.4}$$

In the bilinear form $\tilde{a}(\cdot, \cdot)$, besides the correction term $\int_{\partial\Omega_S} \mu(\mathbf{n}_S \cdot \mathbf{D}(\mathbf{u})\mathbf{n}_S)(\mathbf{v} \cdot \mathbf{n}_S)\,\mathrm{d}s$, there are two more terms in (6.3). The first one, $\int_{\partial\Omega_S} \mu(\mathbf{n}_S \cdot \mathbf{D}(\mathbf{v})\mathbf{n}_S)(\mathbf{u} \cdot \mathbf{n}_S)\,\mathrm{d}s$, is added to maintain symmetry. The second term $\frac{\alpha}{h}\int_{\partial\Omega_S}(\mathbf{u} \cdot \mathbf{n}_S)(\mathbf{v} \cdot \mathbf{n}_S)\,\mathrm{d}s$ is a penalty term that enforces the no-penetration condition $\mathbf{u} \cdot \mathbf{n}_S = 0$ in a weak sense. The parameter $\alpha > 0$ is independent of h and has to be taken sufficiently large. This penalty term is the usual one in Nitsche's method, and it is consistent in the sense that it vanishes if $\mathbf{u}$ is the solution of the continuous problem (which satisfies $\mathbf{u} \cdot \mathbf{n}_S = 0$). Because of this, we have that the error $(\mathbf{u}-\mathbf{u}_h, p-p_h)$ has the usual Galerkin orthogonality property w.r.t. $X_h \times Q_h^\Gamma$.

Using $\boldsymbol{\tau}_L = \frac{\mathbf{P}_\Gamma \mathbf{n}_S}{\|\mathbf{P}_\Gamma \mathbf{n}_S\|}$ and $\mathbf{n}_L = \frac{\mathbf{P}_S \mathbf{n}_\Gamma}{\|\mathbf{P}_S \mathbf{n}_\Gamma\|}$, the right-hand side in (6.4) can be rewritten, and we obtain

$$\tilde{f}_L(\mathbf{u}, \mathbf{v}) = \cos\theta_e \int_L \tau\|\mathbf{P}_S\mathbf{n}_\Gamma\|^{-1}\mathbf{v} \cdot \mathbf{P}_S\mathbf{n}_\Gamma\,\mathrm{d}s + \int_L \|\mathbf{P}_\Gamma\mathbf{n}_S\|^{-1}(\mathbf{n}_S \cdot \boldsymbol{\sigma}_\Gamma\mathbf{n}_S)(\mathbf{v} \cdot \mathbf{n}_S)\,\mathrm{d}s. \tag{6.5}$$

In the latter representation, the (only) geometric information we need is the location of the contact line L, the known normal $\mathbf{n}_S$ and the surface normal $\mathbf{n}_\Gamma$.

Remark 6.1
For the case $\boldsymbol{\sigma}_\Gamma = \boldsymbol{\sigma}_\Gamma^0 = \tau\mathbf{P}_\Gamma$, the formula in (6.5) simplifies to

$$\tilde{f}_L(\mathbf{u}, \mathbf{v}) = \tilde{f}_L^0(\mathbf{v}) := \cos\theta_e \int_L \tau\|\mathbf{P}_S\mathbf{n}_\Gamma\|^{-1}\mathbf{v} \cdot \mathbf{P}_S\mathbf{n}_\Gamma\,\mathrm{d}s + \int_L \tau\|\mathbf{P}_\Gamma\mathbf{n}_S\|\mathbf{v} \cdot \mathbf{n}_S\,\mathrm{d}s. \tag{6.6}$$

7. DISCRETIZATION OF FORCE TERMS

The interface and contact line forces are given by

$$f_\Gamma(\mathbf{u}, \mathbf{v}) = -\int_\Gamma \boldsymbol{\sigma}_\Gamma : \nabla_\Gamma\mathbf{v}\,\mathrm{d}s, \tag{7.1}$$

$$\tilde{f}_L(\mathbf{u}, \mathbf{v}) = \cos\theta_e \int_L \tau\|\mathbf{P}_S\mathbf{n}_\Gamma\|^{-1}\mathbf{v} \cdot \mathbf{P}_S\mathbf{n}_\Gamma\,\mathrm{d}s + \int_L \|\mathbf{P}_\Gamma\mathbf{n}_S\|^{-1}(\mathbf{n}_S \cdot \boldsymbol{\sigma}_\Gamma\mathbf{n}_S)(\mathbf{v} \cdot \mathbf{n}_S)\,\mathrm{d}s. \tag{7.2}$$

We discuss the discretization of these (bi)linear forms. The geometry $\Gamma = \Gamma(t)$ and $L = L(t)$ are approximated as explained in Section 4. For the interface, we use the approximation Γ_h given in (4.3). For the contact line approximation, we take $L_h := \Gamma_h \cap \partial\Omega_S$. Besides the known normal $\mathbf{n}_S$, the only further geometric information we need in (7.1)–(7.2) is the surface normal $\mathbf{n}_\Gamma$. This normal is approximated by $\tilde{\mathbf{n}}_h$, with corresponding projection denoted by $\tilde{\mathbf{P}}_h$, as in (4.4).

For the case $\boldsymbol{\sigma}_\Gamma = \boldsymbol{\sigma}_\Gamma^0 = \tau\mathbf{P}_\Gamma$ (cf. (6.6)), we obtain the following discrete functionals, with $\mathbf{e}_i$ the ith basis vector in $\mathbb{R}^3$:

$$f_{\Gamma,h}^0(\mathbf{v}_h) = -\sum_{i=1}^3 \int_{\Gamma_h} \tau\tilde{\mathbf{P}}_h\mathbf{e}_i \cdot \nabla(\mathbf{v}_h)_i\,\mathrm{d}s \tag{7.3}$$

$$\tilde{f}_{L,h}^0(\mathbf{v}_h) = \cos\theta_e \int_{L_h} \tau\|\mathbf{P}_S\tilde{\mathbf{n}}_h\|^{-1}\mathbf{v}_h \cdot \mathbf{P}_S\tilde{\mathbf{n}}_h\,\mathrm{d}s + \int_{L_h} \tau\|\tilde{\mathbf{P}}_h\mathbf{n}_S\|\mathbf{v}_h \cdot \mathbf{n}_S\,\mathrm{d}s. \tag{7.4}$$

For the case $\boldsymbol{\sigma}_\Gamma = \boldsymbol{\sigma}_\Gamma^{BS}$, similar results are easily obtained. The resulting discrete bilinear forms are denoted by $f_{\Gamma,h}(\mathbf{u}_h, \mathbf{v}_h)$, $\tilde{f}_{L,h}(\mathbf{u}_h, \mathbf{v}_h)$.

8. FULLY DISCRETE PROBLEM

We apply a Rothe approach in which we first apply an implicit Euler method to the fully coupled system of level set and Navier–Stokes equations and then use the methods explained in the previous sections for a spatial discretization. Thus, we obtain the following fully discrete problem, per time step. To simplify the presentation, we assume $\delta_T = \delta_h$ for all $T \in \mathcal{T}_h$ in the SDFEM. Determine $(\mathbf{u}_h^{n+1}, p_h^{n+1}, \phi_h^{n+1}) \in \mathbf{X}_h \times Q_h^\Gamma \times V_h(\phi_D)$ such that

$$
m\left(\frac{\mathbf{u}_h^{n+1} - \mathbf{u}_h^n}{\Delta t}, \mathbf{v}_h\right) + \tilde{a}(\mathbf{u}_h^{n+1}, \mathbf{v}_h) + c(\mathbf{u}_h^{n+1}; \mathbf{u}_h^{n+1}, \mathbf{v}_h) + \tilde{b}(\mathbf{v}_h, p_h^{n+1,\Gamma})
$$
$$
+ \tilde{b}(\mathbf{u}_h^{n+1}, q_h^\Gamma) + \epsilon_p j(p_h^{n+1}, q_h) = f_{ext}(\mathbf{v}_h) + f_{\Gamma,h}(\mathbf{u}_h^{n+1}, \mathbf{v}_h) + \tilde{f}_{L,h}(\mathbf{u}_h^{n+1}, \mathbf{v}_h) \tag{8.1}
$$
$$
\text{for all } \mathbf{v}_h \in \mathbf{X}_h, \ q_h \in Q_h^\Gamma,
$$
$$
\left(\frac{\phi_h^{n+1} - \phi_h^n}{\Delta t} + \mathbf{u}_h^{n+1} \cdot \nabla\phi_h^{n+1}, \psi_h + \delta_h \mathbf{u}_h^{n+1} \cdot \nabla\psi_h\right)_{L^2(\Omega)} = 0, \quad \forall \psi_h \in V_h(0). \tag{8.2}
$$

For the case $\boldsymbol{\sigma}_\Gamma = \boldsymbol{\sigma}_\Gamma^0 = \tau \mathbf{P}_\Gamma$, the discrete force terms $f_{\Gamma,h}$ and $\tilde{f}_{L,h}$ depend only on $\mathbf{v}_h$ and are given in (7.3) and (7.4). We emphasize that through the dependence of $f_{\Gamma,h}$ and $\tilde{f}_{L,h}$ on $\Gamma_h = \Gamma_h(t)$, which is the zero level of $I\phi_h(\cdot, t)$, there is a strong nonlinear coupling between the equations in (8.1) (fluid dynamics) and in (8.2) (interface and contact line dynamics). The decoupling of these two equations is a delicate issue. In the following, we describe two decoupling approaches we used in our simulations. In the first approach (weak coupling), we decouple the computation of (8.1) and (8.2) in each time step. In the second approach (strong coupling), the two equations are solved coupled together by a fixed point iterative method in each step.

Weak coupling. In each time step, we solve (8.1) and (8.2) to get $(\mathbf{u}_h^{n+1}, p_h^{n+1})$ and ϕ_h^{n+1} based on ϕ_h^n and $\mathbf{u}_h^n$ from the previous time step. In each time step, the two subproblems, Navier–Stokes for fluid dynamics and the level set equation for the interface dynamics, are decoupled. This approach is very simple and has relatively low computational costs per time step. In our experiments, this weak coupling performs well in problems where the flow evolves to a stationary one, and one is (mainly) interested in the stationary limit solution. In cases where the solution has a strong dependence on time, it is better to use the following strong coupling approach.

Strong coupling. In the strong coupling algorithm, per time step, we solve (with a certain tolerance) the coupled system (8.1)–(8.2) for the unknowns $(\mathbf{u}_h^{n+1}, p_h^{n+1}, \phi_h^{n+1})$. This is realized by a certain fixed point approach that iterates between the equations in (8.1) and (8.2). In this approach, there is a special semi-implicit treatment of the surface tension force term $f_{\Gamma,h}(\mathbf{u}_h^{n+1}, \mathbf{v}_h)$, with $\Gamma = \Gamma(\phi_h^{n+1})$, which is very important for the rate of convergence of this fixed point iteration. We do not explain this further here, but refer to [40] for more information on the fixed point iteration.

After $(\mathbf{u}_h^{n+1}, p_h^{n+1}, \phi_h^{n+1})$ has been determined, it is checked whether a reinitialization or a volume correction of the level-set function ϕ_h^{n+1} should be determined. Again, because it is outside the scope of this paper, we do not explain these methods, but refer to [40].

9. NUMERICAL EXPERIMENTS

In this section, we apply the solver, outlined in the sections earlier, to a few test problems. We restrict to the interface stress tensor $\boldsymbol{\sigma}_\Gamma = \boldsymbol{\sigma}_\Gamma^0$, and for the contact line force $\mathbf{f}_L$, we restrict to $\beta_L = 0$;

that is, $\mathbf{f}_L = \tau \cos \theta_e \mathbf{n}_L$ (cf. (2.5) except for the experiment in Section 9.3 where we also consider $\beta_L > 0$).

We summarize the main components of the solver:

- We use a modified P_2-P_1 Hood–Taylor pair for the spatial discretization of the Navier–Stokes equation. The modification is that instead of P_1 for the pressure we use the stabilized P_1-XFEM discretization. We use a hierarchy of tetrahedral grids, which are locally refined close to the (moving) interface.
- We use the level set method for interface capturing. For the spatial discretization of the level set equation, we use a standard SDFEM with P_2 finite elements. In this level set method, it is essential to use a suitable reparametrization technique (which is not explained in this paper).
- For the evaluation of surface tension and contact line forces, we use a piecewise linear reconstruction of the interface. These forces are discretized as in (7.3) and (7.4).
- We use Nitsche's method for handling the Navier boundary condition, resulting in a modified bilinear form as in (6.3).

In the test problems considered in Section 9.1, we use the weak coupling in the time integration, whereas in all other test problems, we use the strong coupling.

9.1. Static droplet on a plate

In two-phase incompressible flow simulations without contact line, a system with a static droplet is often used as a first test for the accuracy of the two-phase flow solver. In this basic test problem, the quality of the discretization of surface tension forces and of the discontinuous pressure solution can be verified. We consider such a static droplet problem *with* contact line. The test problem has a static droplet with radius $R = 0.1$ on a planar surface in a cubic domain $\Omega = (0, 0.5)^3$. The initial contact angle θ_0 is set to equal to the prescribed equilibrium angle $\theta_e = 60°$. We assume a constant surface tension coefficient $\tau = 0.5$. The densities and viscosities of both fluids are set to 1, and we set gravity to 0. On the whole boundary, we assume a Navier slip condition with $\beta_S = 0.05$.

This problem has the stationary solution

$$\mathbf{u}^* = 0 \text{ in } \Omega_1 \cup \Omega_2, \qquad p^* = \begin{cases} c_0 + k_{\text{const}} & \text{in} \Omega_1 \\ c_0 & \text{in } \Omega_2 \end{cases}$$

where $k_{\text{const}} = \frac{2\tau}{R} = 10$. Because of the discretization of the surface tension forces and the approximation of the pressure solution p^* in the finite element space, spurious velocities will appear. The accurate Laplace–Beltrami approach in the discretization (7.3) and the use of the XFEM method for the pressure approximation result in very small spurious velocities. In Figures 3 and 4, we illustrate the sharp pressure jump.

We investigate the convergence behavior of the discrete solution pair $(\mathbf{u}_h, p_h)$. Results are presented in the Table I. The initial level 0 grid is obtained from a uniform tetrahedral grid that has only five vertices (four intervals) on each edge of the cube Ω, which is then locally refined once close to the interface. Hence, on level 0, the tetrahedra close to the interface have edges of length $0.5 * (\frac{1}{2})^3 = \frac{1}{16}$. An increase in the level number (first column) in this table corresponds to a local refinement close to the interface of the tetrahedral grid (i.e., one regular local refinement followed by a correction step for elimination of hanging nodes). In Figure 3, a cross section of the level 4 mesh is shown. One important contribution of this paper is the application of the stabilized XFEM method to this problem class. From experiments, it follows that the behavior of this method is very satisfactory. In particular, there is no strong sensitivity with respect to the choice of the stabilization parameter ϵ_p in (8.1). To illustrate this, we present results for $\epsilon_p = 1$ and for $\epsilon_p = 0.01$. For these two values of ϵ_p, the discrete velocities do not show significant differences, and therefore, we only show the errors for the case $\epsilon_p = 1$. We observe only a mild deterioration of the pressure quality if the stabilization parameter is reduced from $\epsilon_p = 1$ to $\epsilon_p = 0.01$.

An important conclusion is that these results show a very good agreement with results from a similar experiment *without a contact line*, see section 7.10 in [40]. Hence, the numerical treatment of the contact line force and of the Navier boundary condition is satisfactory (in this test problem).
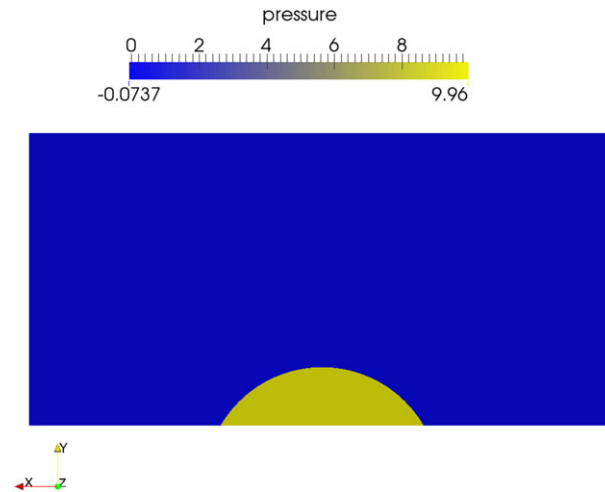
Figure 3. A cross section of the pressure approximation on a locally refined mesh. [Colour figure can be viewed at wileyonlinelibrary.com]
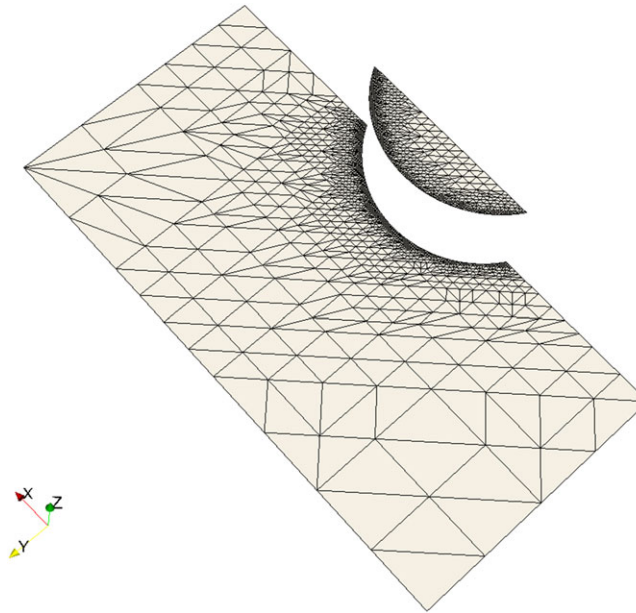

Figure 4. The pressure jump is visualized by scaling in the normal direction of the cross section. [Colour figure can be viewed at wileyonlinelibrary.com]

Table I. Convergence behavior for a static droplet on a plate with $\theta_e = 60°$ and different values $\epsilon_p = 1, 10^{-2}$ in the XFEM stabilization.

Mesh level	$\|e_u\|_{L_2}, \epsilon_p = 1$	Order	$\|e_p\|_{L_2}, \epsilon_p = 1$	Order	$\|e_p\|_{L_2}, \epsilon_p = 0.01$	Order
0	6.79E-5	—	5.37E-3	—	5.31E-3	—
1	1.54E-5	2.14	1.24E-3	2.13	1.34E-3	1.97
2	3.18E-6	2.28	3.38E-4	1.87	3.89E-4	1.79
3	7.33E-7	2.12	8.53E-5	1.99	1.09E-4	1.85
4	1.69E-7	2.12	8.53E-5	1.99	1.09E-4	1.85
5	4.08E-8	2.05	5.78E-6	1.93	1.04E-5	1.67
6	1.00E-8	2.03	1.57E-6	1.89	3.63E-6	1.52

The (very small) errors in velocity are caused by spurious velocities close to the interface. The suboptimal order of convergence in velocity is caused by the errors in the discretization of the surface tension force [55]. As a further error measure, a numerical contact angle θ_h is determined and compared with the exact one, θ_e. The numerical contact angle θ_h is defined as the average of the local (per tetrahedron) approximate angles that are obtained from the level set function normals (4.4). In a similar way, a discrete radius r_h, which approximates r, is determined. The results are given in Table II and show (approximately) the expected second order convergence.

9.2. A droplet sliding to equilibrium state

We extend the previous test case in Section 9.1 to a non-stationary problem. We take the same setup as described in Section 9.1 except that we take the initial contact angle $\theta_0 = 90°$ and take different equilibrium contact angles $\theta_e \neq \theta_0$. We consider the three cases $\theta_e = 30°, \theta_e = 60°$, and $\theta_e = 120°$ (cf. Figure 5). When we release the droplet with initial contact angle θ_0, it will spread or contract to a spherical cap with contact angle θ_e.

The time dependent solution of this problem converges to a static state, which is known (essentially the same as in the static droplet case). Note that in this test case we have an evolving interface (and contact line), and thus, the level set method and its coupling with the Navier–Stokes equations play a key role.

By using conservation of volume of the droplet, we can calculate the radius of the droplet R and the radius r of the circle inside the contact line at the static state. For the 3D case, we thus obtain, with R_0 the droplet radius at $t = 0$,

$$R = R_0 \sqrt[3]{\frac{2}{2 - 2\cos\theta_e - \sin^2\theta_e \cos\theta_e}}, \quad r = R\sin\theta_e. \tag{9.1}$$

(In [8] the 2D analogon of this formula is given).

We perform a simulation until the equilibrium is reached (approximately). For the numerical equilibrium solution, we determine a numerical contact angle θ_h and discrete radius in the same way as in the static droplet case earlier. The corresponding (relative) errors on mesh level 1, which has the same resolution as the level 1 mesh in the previous experiment, are shown in Table III. We note that in this experiment, because of the dynamics of the interface, the locally refined grid is changing in time during the simulation (local grid refinement and coarsening).

Comparing the results in Table III with the level 1 results in Table II, we see that the errors have the same order of magnitude. The errors in velocity and pressure for the numerical equilibrium

Table II. Errors in approximation of contact angle θ and radius r.

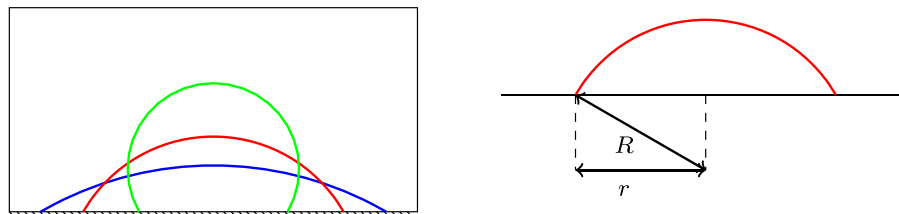| Mesh level	$|\theta_h - \theta_e|/\theta_e$	Order	$|r - r_h|/r$	Order
0	3.07E-2	—	1.44E-2	—
1	1.06E-2	1.53	3.42E-3	2.08
2	2.46E-3	2.11	8.16E-4	2.07
3	4.75E-4	2.37	2.09E-4	1.97
4	1.31E-4	1.85	5.19E-5	2.01

Figure 5. 2D sketch of the static droplet shape and of the radii R and r. [Colour figure can be viewed at wileyonlinelibrary.com]

Table III. Errors in contact angle θ_e and radius r for three cases on the level 1 mesh.

θ_e	θ_h	$|\theta_h - \theta_e|/\theta_e$	r	r_h	$|r_h - r|/r$
30°	29.77°	7.7E-3	0.169384	0.169425	2.42E-4
60°	59.74°	4.3E-3	0.127619	0.127408	1.65E-3
120°	119.6°	3.3E-3	0.0727416	0.0733349	8.15E-3

solution on mesh level 1 are $\|e_u\|_{L^2} = 2.03\text{E-}6$ and $\|e_p\|_{L^2} = 1.13\text{E-}3$. These are of the same order of magnitude (or even smaller) as the level 1 errors in Table I. From this, we conclude that these results for the time dependent simulation are very satisfactory. Under mesh refinement, we observe convergence which, however, does not show a regular second order behavior. This is caused by an undesirable behavior of the reparametrization and volume correction method, which is not addressed in this paper.

9.3. Dynamics of sliding droplets

In this experiment, we illustrate an important difference between the models with $\beta_L = 0$ and $\beta_L > 0$ in (2.5) (or in the contact line balance Equation (2.12)), which is also noted in the papers [20, 27].

The test problem that we consider has a droplet with radius $R = 0.1$ at $t = 0$ on a planar surface in a cubic domain $\Omega = (0, 0.5)^3$. We take the initial contact angle $\theta_0 = 90°$ and an equilibrium contact angle $\theta_e = 60°$. We assume a constant surface tension coefficient $\tau = 0.4$. The initial velocity is $\mathbf{u} = 0$. Densities and viscosities are taken as $\rho_1 = \mu_1 = 2$, $\rho_2 = \mu_2 = 1$. On the whole boundary, we assume a Navier slip condition with $\beta_S = 0.5$.

We performed a droplet spreading simulation on four mesh levels. The setup of mesh levels is the same as in Section 9.1. For β_L, we take the values $\beta_L = 0$ and $\beta_L = 20$. We consider the dynamics of the (numerical) contact angle θ_h and the (numerical) contact radius r_h. Results are shown in Figures 6 and 7. Note that different colors correspond to different mesh levels. The results for the model with $\beta_L = 0$ are plotted with dashed lines and the results for $\beta_L = 20$ with solid lines.

In Figure 6, we observe that the dynamics of the contact angle in the GNBC model ($\beta_L = 0$) has a strong mesh-dependent behavior at the beginning of the simulations, in agreement with the results in [20, 27]. This is because the GNBC model is essentially a quasi-static contact angle model. For $\beta_L = 20$, we observe a regular convergence (for decreasing mesh size) of $\theta_h(t)$ to a contact angle $\theta(t)$ with a smooth dynamics. For the contact radius $r_h(t)$, we observe convergence (for decreasing mesh size) to a smoothly varying limit solution $r(t)$ in both cases $\beta_L = 0$ and $\beta_L = 20$. We obtain accurate numerical simulation results for both models, within our unified simulation framework. As emphasized before, we do not address the quality and range of validity of the two models ($\beta_L = 0$ and $\beta_L = 20$).

9.4. Couette flow

In this section, we do a further validation of the solver by considering a two-phase Couette flow in a 3D channel $[0, L_x] \times [0, L_y] \times [0, L_z]$ with MCL. In the first experiment, the two fluids are separated by two different interfaces, whereas in the second experiment (cf. Figure 10), there is only one interface between the fluids. The upper and lower boundaries are walls that move with velocity U_{wall} and $-U_{wall}$ in x-direction, respectively.

We show results of two types of numerical experiments. First we present results obtained with our solver and study grid convergence by using a reference solution that is obtained by applying the solver on a very fine grid. In the second experiment, we compare the simulation results of our solver with MD simulation results from the literature. In both cases, we set $\theta_0 = \theta_e = 90°$.

Convergence study with a fine mesh reference solution. The setup is as described earlier, with a Navier boundary condition on the upper and lower (moving) boundaries, a periodic boundary
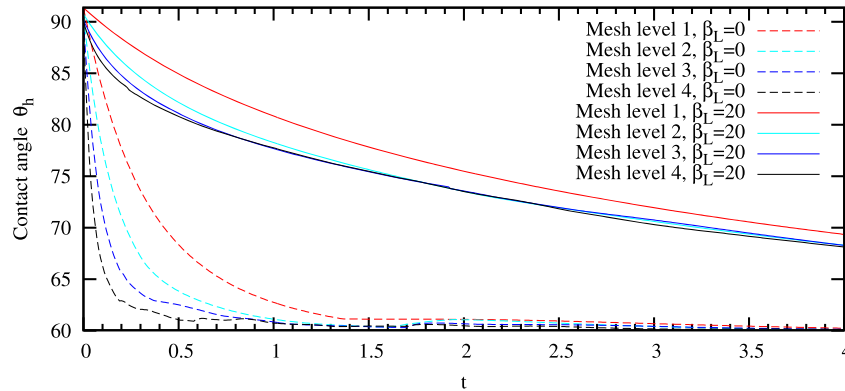
Figure 6. Numerical contact angle $\theta_h(t)$ on different mesh levels for $\beta_L = 0$ and $\beta_L = 20$.
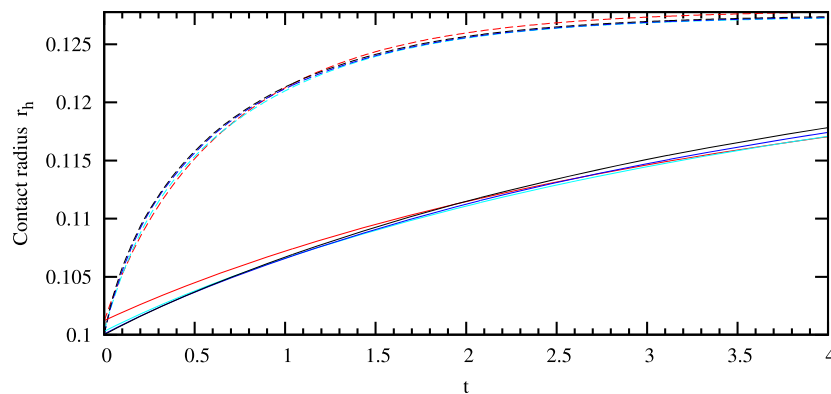

Figure 7. Numerical contact radius $r_h(t)$ on different mesh levels for $\beta_L = 0$ and $\beta_L = 20$.

condition on left and right boundaries and a symmetry boundary condition in y-direction. We take length $L_x = 1$, width $L_y = 0.2$, and height $L_z = 0.4$.

The initial velocity is $\mathbf{u} = 0$. Densities and viscosities are taken as $\rho_1 = \mu_1 = 3$, $\rho_2 = \mu_2 = 1$. The slip coefficient in the effective wall force $\mathbf{f}_S$ is set to $\beta_S = 1.2$, and the surface tension coefficient is $\tau = 5.5$. These two parameter values are the same as in the MD simulations from [6], which are considered in the next experiment. In this test, we take an initial uniform tetrahedral triangulation with five vertices (four intervals) on the edges of the channel in x-direction, three vertices (two intervals) on the edges in z-direction, and two vertices (one interval) on the edges in y-direction. We use uniform refinement. The (technical) reason for this is that with uniform refinement the interpolation of coarse grid functions to finer grids is obvious, and there are no interpolation errors. For $t = 0.032$, we compute a reference solution $\mathbf{u}^{Ref}$ on the tetrahedral triangulation obtained after five refinements of the initial one. We use such a short time interval $[0, 0.032]$ because of computational limitations for computing the reference solution on the five times refined triangulation. For $t = 0.032$, the velocity solution as a size $\|\mathbf{u}^{Ref}\|_{L^2} = 8.76E-2$. The velocity errors on coarser grids (for $t = 0.032$) are shown in Table IV. We observe that on average we get a close to 1.5 order of convergence for the velocity. Furthermore, note that after one refinement we have a relatively coarse mesh but already a rather accurate numerical solution. To illustrate this, in Figure 8, we show a line plot of the x-velocity in x–z plane at $y = 0.1$ from the point $(x, z) = (0, 0)$ to the point $(x, z) = (1, 0.4)$ for the reference mesh and the level 1 mesh. In Figure 9, we show a cross section at $y = 0.1$ of the computed solution on a 2 times refined triangulation at $t = 0.032$.

Comparison with MD simulation. We performed a second numerical simulation experiment for the Couette flow in which results are compared with MD simulations in [6].

Table IV. The convergence behavior of velocity.

Ref.	$\|\mathbf{u}^{Ref} - \mathbf{u}_h\|_{L_2}$	Order
0	8.6E-3	—
1	2.5E-3	1.8
2	1.3E-3	0.94
3	4.4E-4	1.6
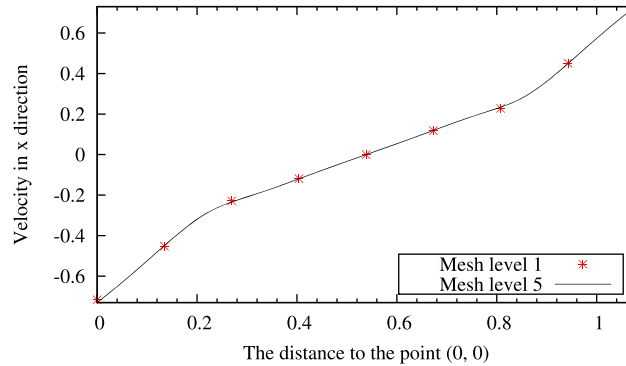
Figure 8. The velocity in x direction from the point $(x, z) = (0, 0)$ to the point $(x, z) = (1, 0.4)$ in x–z plane at $t = 0.032$. [Colour figure can be viewed at wileyonlinelibrary.com]
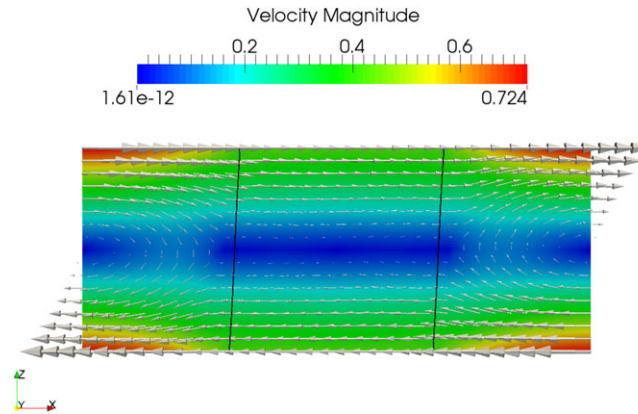
Figure 9. The Couette flow at $t = 0.032$, on a 2 times refined triangulation. [Colour figure can be viewed at wileyonlinelibrary.com]

The MD setup from [6] is shown in Figure 10. It is a 3D channel with length $L_x = 163.5\sigma$, width $L_y = 6.8\sigma$, and height $L_z = 13.6\sigma$, where σ is the relevant unit (a microscopic length scale in the MD simulation). Note that opposite to the previous experiment, there is *one* interface between two immiscible fluids in the middle of the channel. The density of the two fluids are $\rho_1 = \rho_2 = 0.81m/\sigma^3$, and their viscosities are $\mu_1 = \mu_2 = 1.95\sqrt{m\epsilon}/\sigma^2$, where m and ϵ are suitable mass and energy scales in the MD simulation. From now on, we delete the units. The slip coefficient in the effective wall force is set to $\beta_S = 1.2$. The surface tension is $\tau = 5.5$. The wall velocity is $U_{wall} = 0.25$. In this system, a steady state is reached as illustrated in Figure 10.

The MD simulations provide velocity profiles, which will be compared with the numerical simulations by our finite element method. In our simulations, we take the channel given by $(-L_x/2, L_x/2) \times (0, L_y) \times (0, L_z)$, and we use a periodic boundary condition in the y-direction. On the left and right boundaries, we take Dirichlet boundary condition given by $\mathbf{u}(y, z) = \frac{2U_{wall}(z - L_z/2)}{L_z + 2*l_s}\mathbf{e}_1$, for $(y, z) \in (0, L_y) \times (0, L_z)$, where $l_s = \mu/\beta_S$ is the slip length.
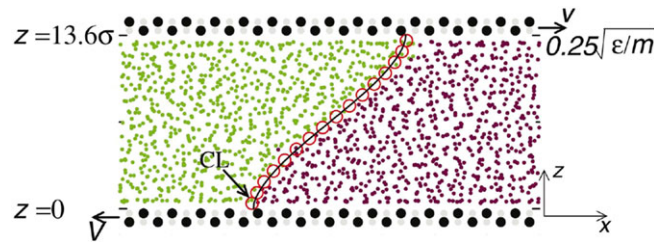
Figure 10. The MD Couette flow setup in [6]. [Colour figure can be viewed at wileyonlinelibrary.com]
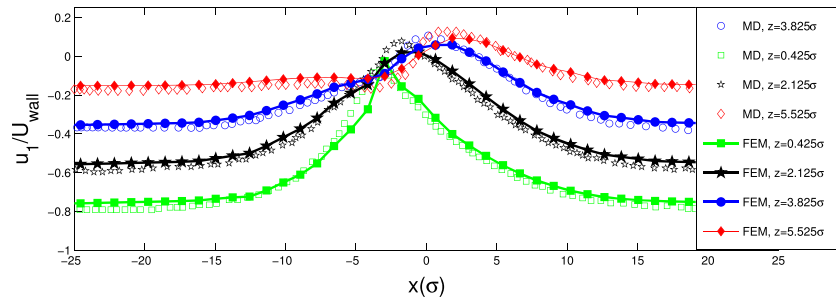

Figure 11. Comparisons of MD simulations and the sharp-interface model simulations. [Colour figure can be viewed at wileyonlinelibrary.com]

In this test, we take an initial tetrahedral triangulation with 11 vertices (10 intervals) on the edges of the channel in x-direction, five vertices (four intervals) on the edges in z-direction, and three vertices (two interval) on the edges in y-direction, and we apply three adaptive refinements near the interface.

Numerical results for the computed equilibrium solution are shown in Figure 11. We show the profile of the relative velocity in x-direction u_1/U_{wall}, where u_1 denotes the x-component of velocity. The profiles are shown for $u_1(x, \frac{1}{2}L_y, z_j)$, with $x \in [-25, 25]$, $z_1 = 0.425$ (green/bottom), $z_2 = 2.125$ (black), $z_3 = 3.825$ (blue), and $z_4 = 5.525$ (red/top). The empty symbols show the results from MD simulations, and the filled symbols with solid lines show the results by our FEM method. We observe a good agreement between the two sets of simulation results. Note that differences may be due not only to numerics but also to modeling discrepancies. Near the wall boundary, at $z_1 = 0.425$ (bottom curve), the x-velocity $u_1(x, \frac{1}{2}L_y, z_1)/U_{wall}$ is close zero for x close to the contact line, which implies that the fluids slip there (note that the wall moves).

10. CONCLUSION AND OUTLOOK

We presented a general variational formulation for a class of two-phase sharp interface models with MCL in which the interface and contact line force balances are treated as natural conditions. A level set based finite element discretization method is treated. A unified approach for discretization of different interface stress tensors σ_Γ and contact line forces $\mathbf{f}_L$ is discussed. The stabilized XFEM method, recently introduced in [31] for a stationary two-phase Stokes problem, is applied for this two-phase flow problem with MCL. The Nitsche method is used for a flexible and accurate handling of the Navier boundary condition. A further study of these methods by numerical analyses, application to more challenging applications, and comparison with other numerical approaches is planned. We also consider a systematic model validation, using the finite element solver presented in this paper, as an interesting topic for further research.

REFERENCES

1. Huh C, Scriven L. Hydrodynamic model of steady movement of a solid/liquid/fluid contact line. *Journal of Colloid and Interface Science* 1971; **35**:85–101.
2. Cox R. The dynamics of the spreading of liquids on a solid surface. Part 1. Viscous flow. *Journal of Fluid Mechanics* 1986; **168**:169–194.
3. Shikhmurzaev Y. The moving contact line on a smooth solid surface. *International Journal of Multiphase Flow* 1993; **19**(4):589–610.
4. Jacqmin D. Contact-line dynamics of a diffuse fluid interface. *Journal of Fluid Mechanics* 2000; **402**:57–88.
5. Yue P, Zhou C, Feng JJ. Sharp-interface limit of the Cahn–Hilliard model for moving contact lines. *Journal of Fluid Mechanics* 2010; **645**:279–294.
6. Qian T, Wang X-P, Sheng P. Molecular scale contact line hydrodynamics of immiscible flows. *Physical Review E* 2003; **68**:1–15.
7. Ren W, E W. Boundary conditions for the moving contact line problem. *Physics of Fluids* 2007; **19**:1–15.
8. Dupont J-B, Legendre D. Numerical simulation of static and sliding drop with contact angle hysteresis. *Journal of Computational Physics* 2010; **229**:2453–2478.
9. Snoeijer J, Andreotti B. Moving contact lines: scales, regimes, and dynamical transitions. *Annual Review of Fluid Mechanics* 2013; **45**:269–292.
10. Sui Y, Ding H, Spelt PDM. Numerical simulations of flows with moving contact lines. *Annual Review of Fluid Mechanics* 2014; **46**:97–119.
11. Renardy M, Renardy Y, Li J. Numerical simulation of moving contact line problems using a volume-of-fluid method. *Journal of Computational Physics* 2001; **171**:243–263.
12. Spelt PDM. A level-set approach for simulations of flows with multiple moving contact lines with hysteresis. *Journal of Computational Physics* 2005; **207**:389–404.
13. Gao M, Wang X-P. A gradient stable scheme for a phase field model for the moving contact line problem. *Journal of Computational Physics* 2012; **231**:1372–1386.
14. Bao K, Shi Y, Sun S, Wang X-P. A finite element method for the numerical solution of the coupled Cahn–Hilliard and Navier–Stokes system for moving contact line problems. *Journal of Computational Physics* 2012; **231**:8083–8099.
15. Sui Y, Spelt PDM. An efficient computational model for macroscale simulations of moving contact lines. *Journal of Computational Physics* 2013; **242**:37–52.
16. Sprittles J, Shikhmurzaev Y. Finite element simulation of dynamic wetting flows as an interface formation process. *Journal of Computational Physics.* 2013; **233**:34–65.
17. Gao M, Wang X-P. An efficient field model for the moving contact line problem with variable density and viscosity. *Journal of Computational Physics* 2014; **272**:704–718.
18. Xu J-J, Ren W. A level-set method for two-phase flows with moving contact line and insoluble surfactant. *Journal of Computational Physics* 2014; **263**:71–90.
19. Shen J, Yang X, Yu H. Efficient energy stable numerical schemes for a phase field moving contact line model. *Journal of Computational Physics* 2015; **284**:617–630.
20. Buscaglia GC, Ausus RF. Variational formulations for surface tension, capillarity and wetting. *Computer Methods in Applied Mechanics and Engineering* 2011; **200**:3011–3025.
21. Legendre D, Maglio M. Numerical simulation of spreading drops. *Colloids and Surfaces A: Physicochemical and Engineering Aspects* 2013; **432**:29–37.
22. Ren W, Hu D, E W. Continuum models for the contact line problem. *Physics of Fluids* 2010; **22**:1–19.
23. Zhang Z, Xu S, Ren W. Derivation of a continuum model and the energy law for moving contact lines with insoluble surfactants. *Physics of Fluids* 2014; **26**:1–19.
24. Sikalo S, Wilhelm H-D, Roisman IV, Jakirlic S, Tropea C. Dynamic contact angle of spreading droplets: experiments and simulations. *Physics of Fluids* 2005; **17**:1–13.
25. Yokoi K, Vadillo D, Hinch J, Hutchings I. Numerical studies of the influence of the dynamic contact angle on a droplet impacting on a dry surface. *Physics of Fluids* 2009; **21**:1–12.
26. Afkhami S, Zaleski S, Bussmann M. A mesh-dependent model for applying dynamic contact angles to VOF simulations. *Journal of Fluid Mechanics, Journal of Computational Physics* 2009:5370–5389.
27. Ganesan S, Tobiska L. Modelling and simulation of moving contact line problems with wetting effects. *Computing and Visualization in Science* 2009; **12**:329–336.
28. Ganesan S. On the dynamic contact angle in simulation of impinging droplets with sharp interface methods. *Microfluidics and nanofluidics* 2013; **14**(3-4):615–625.
29. Manservisi S, Scardovelli R. A variational approach to the contact angle dynamics of spreading droplets. *Computers and Fluids* 2009; **38**:406–424.
30. Walker S, Bonito A, Nochetto R. Mixed nite element method for electrowetting on dielectric with contact line pinning. *Interfaces and Free Boundaries* 2010; **12**:85–119.
31. Hansbo P, Larson M, Zahedi S. A cut finite element method for a Stokes interface problem. *Applied Numerical Mathematics* 2014; **85**:90–114.
32. Urquiza J, Garon A, Farinas M-I. Weak imposition of the slip boundary condition on curved boundaries for Stokes flow. *Journal of Computational Physics* 2014; **256**:748–767.
33. Slattery J, Sagis L, Oh E-S. *Interfacial Transport Phenomena* (Second ed.) Springer: New York, 2007.

34. Sagis L. Dynamic properties of interfaces in soft matter: experiments and theory. *Reviews of Modern Physics* 2011; **83**:1367–1403.
35. Blake T. The physics of moving wetting lines. *Journal of Colloid and Interface Science* 2006; **299**:1–13.
36. Bonn D, Eggers J, Indekeu J, Meunier J, Rolley E. Wetting and spreading. *Reviews of Modern Physics* 2009; **81**: 739–805.
37. Qian T, Wang X-P, Sheng P. A variational approach to moving contact line hydrodynamics. *Journal of Fluid Mechanics* 2006; **564**:333–360.
38. Ren W, E W. Derivation of continuum models for the moving contact line problem based on thermodynamic principles. *Communications in Mathematical Sciences* 2011; **9**:597–606.
39. Shikhmurzaev YD. Moving contact lines in liquid/liquid/solid systems. *Journal of Fluid Mechanics* 1997; **334**: 211–249.
40. Gross S, Reusken A. *Numerical Methods for Two-phase Incompressible Flows*, Springer Series in Computational Mathematics, vol. 40. Springer: Heidelberg, 2011.
41. Gerbeau J-F, Lelievre T. Generalized Navier boundary condition and geometric conservation law for surface tension. *Computer Methods in Applied Mechanics and Engineering* 2009; **198**:644–656.
42. Bänsch E, Morin P, Nochetto R. A finite element method for surface diffusion: the parametric case. *Journal of Computational Physics* 2005; **203**:321–343.
43. Deckelnick K, Dziuk G, Elliott C. Computation of geometric partial differential equations. *Acta Numerica* 2005:139–232.
44. Gross S, Reusken A. Finite element discretization error analysis of a surface tension force in two-phase incompressible flows. *SIAM Journal on Numerical Analysis* 2007; **45**:1679–1700.
45. Ausus R, Sousa F, Buscaglia G. An improved finite element space for discontinuous pressures. *Computer Methods in Applied Mechanics and Engineering* 2010; **199**:1019–1031.
46. Hysing S. A new implicit surface tension implementation for interfacial flows. *International Journal for Numerical Methods in Fluids* 2006; **51**:659–672.
47. Saksono P, Peric D. On finite element modelling of surface tension. *Computational Mechanics* 2006; **38**:265–281.
48. Reusken A, Zhang Y. Numerical simulation of incompressible two-phase flows with a Boussinesq-Scriven surface stress tensor. *Journal for Numerical Methods in Fluids* 2013; **73**:1042–1058.
49. Roos H-G, Stynes M, Tobiska L. *Numerical Methods for Singularly Perturbed Differential Equations — Convection-Diffusion and Flow Problems* (second ed.), Springer Series in Computational Mathematics, vol. 24. Springer-Verlag: Berlin, 2008.
50. Sethian J. A fast marching level set method for monotonically advancing fronts. *Proceedings of the National Academy of Sciences of the United States of America*, Vol. 93, USA, 1996; 1591–1595.
51. Reusken A. Analysis of an extended pressure finite element space for two-phase incompressible flows. *Computer Vision Science* 2008; **11**:293–305.
52. Sauerland H, Fries T. The extended finite element method for two-phase and free-surface flows: a systematic study. *Journal of Computational Physics* 2011; **230**:3369–3390.
53. Hansbo P. Nitsche's method for interface problems in computational mechanics. *GAMM-Mitteilungen* 2005; **28**(2):183–206.
54. Nitsche J. Über ein Variationsprinzip zur Lösung von Dirichlet-Problemen bei Verwendung von Teilräumen, die keinen Randbedingungen unterworfen sind. *Abhandlungen aus dem Mathematischen Seminar der Universität Hamburg* 1971; **36**:9–15.
55. Grande J. Finite element discretization error analysis of a general interfacial stress functional. *SIAM Journal on Numerical Analysis* 2015; **53**:1236–1255.